Widening the field-of-view of Very Long Baseline Interferometric surveys through advanced calibration techniques

By

Llewellyn Victor COETZER

UNIVERSITEIT VAN PRETORIA
UNIVERSITY OF PRETORIA
YUNIBESITHI YA PRETORIA
Denkleiers • Leading Minds • Dikgopolo tša Dihlalefi

Department of Physics
UNIVERSITY OF PRETORIA

Submitted in fulfilment of the requirements for the degree of MASTER OF SCIENCE (MSC) IN PHYSICS in the Faculty of Natural and Agricultural Sciences.

May 3, 2025

Supervisor: Dr. Jack F. RADCLIFFE

UNIVERSITY OF PRETORIA

Abstract

Faculty of Natural and Agricultural Sciences
Department of Physics

Master of Science (MSc) in Physics

Widening the field-of-view of Very Long Baseline Interferometric surveys through advanced calibration techniques

by Llewellyn Victor COETZER

Supervisor: Dr. Jack F. RADCLIFFE

Keywords: Instrumentation: interferometers, Methods: analytical, Methods: numerical, Techniques: interferometric

Very long baseline interferometry (VLBI) is a vital tool in astronomy that unlocks extremely high resolutions with high sensitivity. The fields of view (FoVs) of VLBI observations historically were limited by bandwidth and time smearing, as well as signal attenuation experienced by the array elements due to their primary beams. Technological upgrades and improved correlation and calibration techniques have largely eliminated smearing, leaving the primary beams as the last major FoV restriction. In this thesis, we derive primary beam models for a large subset of antennas in the European VLBI Network (EVN) and *enhanced* Multi-Element Radio Linked Interferometer Network (*e*-MERLIN) using an observation scheme similar to out-of-focus holography (OOF). These models are also applied to a wide-field observation of the Hubble Deep Field-North (HDFN) to test their efficacy in removing beam-related attenuation. Obtaining accurate primary beam models of the antennas in VLBI networks would allow for wide-field observations' development to accelerate and unlock many new facets of science, including active galactic nuclei (AGN) surveys, AGN feedback studies, gravitational lens surveys, and interstellar medium density studies, to only mention a few. In this project, we also face the additional challenge of modelling heterogeneous arrays, meaning that different primary beams are present in the data.

Declaration of Authorship

I, Llewellyn Victor COETZER, declare that the thesis, which I hereby submit for the degree of MSc in Physics at the University of Pretoria, is my own work and has not previously been submitted by me for a degree at this or any other tertiary institution.

Signature: 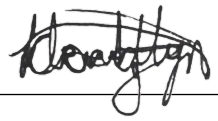

Date: 3 May 2025

"If I have seen further it is by standing on the shoulders of Giants."

Isaac Newton

Acknowledgements

I wish to extend my gratitude to my supervisor, Dr. Jack F. RADCLIFFE, for inspiring me to pursue astronomy and for providing invaluable guidance, insight, and moral support throughout my research journey. His profound knowledge and extensive experience have been instrumental in overcoming the challenges encountered over the past two years, and I remain in awe of his expertise in this field of science.

I am thankful to the University of Pretoria for awarding me the UP Postgraduate Master's Research Bursary. This financial support was not only a significant source of motivation to persevere and complete my studies but also enabled me to upgrade my computer, thereby enhancing the efficiency of my research and studies.

I am profoundly grateful to my family for their unwavering financial and emotional support throughout my academic journey. Their sacrifices, guidance, and encouragement have provided me with a strong foundation and direction in life, and I hope this achievement makes them proud. I especially thank them for their patience and for always being willing to listen to my enthusiastic explanations of the challenges I encountered during this research.

I also wish to acknowledge my friends, who have been a vital part of my support system. Their curiosity about my studies and research and their encouragement have been a source of motivation and positivity during this process.

My gratitude extends to the pioneering scientists who developed the fields of physics and radio astronomy to their current state. Their contributions laid the groundwork for my research and continue to inspire me. This inspiration is also reflected in the quote I have chosen to include in this thesis. Lastly, I wish to thank Prof. Kip S. Thorne for his book Black Holes & Time Warps: Einstein's Outrageous Legacy. This work profoundly influenced my educational journey, igniting my passion for physics and shaping my desire to study it.

Furthermore, I acknowledge the use of the ilifu cloud computing facility - www.ilifu.ac.za, a partnership between the University of Cape Town, the University of the Western Cape, Stellenbosch University, Sol Plaatje University, the Cape Peninsula University of Technology and the South African Radio Astronomy Observatory. The ilifu facility is supported by contributions from the Inter-University Institute for Data Intensive Astronomy (IDIA - a partnership between the University of Cape Town, the University of Pretoria and the University of the Western Cape), the Computational Biology division at UCT and the Data Intensive Research Initiative of South Africa (DIRISA).

Contents

List of Figures

List of Tables

Chapter 1

Introduction

Very Long Baseline Interferometry (VLBI) has become one of the most important fields of astronomy since its inception in the late 1960s (Thompson, Moran, and Swenson, 2017). It has been used in every major astronomy field, including cosmology, supernova remnant studies, fast radio burst (FRB) localisation studies, interstellar medium (ISM) studies, and the most prominent VLBI field, active galactic nuclei (AGN) studies (Venturi et al., 2020). VLBI can be seen as interferometry on a global scale where the baselines are thousands of kilometres long. This makes it useful, as the long baselines lead to high resolutions and surface brightness temperature requirements. These attributes make VLBI ideal for AGN detection due to their compact size and general brightness. VLBI is also unaffected by dust around AGN due to the wavelengths it operates in.

The obtainable fields of view (FoVs) of VLBI observations were historically limited by computational power and correlation and calibration techniques of the time, which lead to bandwidth and time smearing (Garrett et al., 1999; Middelberg and Bach, 2008). The vast improvements seen recently in available computational power led to finer time and bandwidth resolutions becoming available, which, when coupled with the advent of software correlators (see Deller et al., 2007; Deller et al., 2011) and modern correlation and calibration methodologies, have essentially lifted these restrictions.

A third FoV-restricting factor, which historically could be largely ignored, is the attenuation in signals measured by the antennae caused by their response patterns (Middelberg and Bach, 2008). For modern VLBI arrays, this is the last factor that stands in the way of regular wide-field observations, which are observations with FoVs reaching the outskirts of the primary beams of the antennae involved. Solving this problem is thus the next logical step in developing VLBI further, as wide-field observations can unlock more information in gravitational lensing studies (such as Spingola et al., 2019), ISM studies (Morgan et al., 2013), and AGN studies (Middelberg et al., 2011), to name only a few. These observations are also key to successful and timely VLBI sky surveys such as the Square Kilometer Array Pathfinder Radio Continuum Surveys (SPARCS, Njeri et al., 2022) and the survey by Radcliffe et al.

(2018) covering the northern regions of the Hubble Space Telescope's Great Observatories Origins Deep Survey (GOODS-N). The elimination of the response-induced signal attenuation would allow wide-field observations to be routinely conducted, which in turn would expand the sphere of VLBI science substantially.

In this thesis, we aim to derive models of this attenuation for antennae in the European VLBI Network (EVN) and the *enhanced* Multi-Element Radio Linked Interferometer Network (*e*-MERLIN) and apply them to observational data to attempt to assess their accuracy and efficacy in eliminating the attenuation. In the rest of this chapter, we will introduce the topics of this thesis, starting with the mathematical foundation of VLBI. In Chapter 2, we discuss the primary beams of antennae and the application of models to remove attenuation in the data. Chapter 3 discusses the observations relevant to this thesis and the data calibration steps taken. In Chapter 4, we give the results, followed by a discussion in Chapter 5. In Chapter 6, we apply the newly derived models to the EVN observation EG078B and discuss the results. Finally, our conclusions and suggestions for future work are given in Chapter 7.

1.1 VLBI

In VLBI, the signals measured by each antenna are averaged into time- and frequency steps and then multiplied with the signals of the other antennae in the observation in a pairwise fashion (Thompson, Moran, and Swenson, 2017). This process is called correlation, the outputs of which are called visibilities. These visibilities have a distinct relationship with the distribution of electromagnetic radiation in the sky where the observation was focused on, derived from the van Cittert-Zernike theorem (van Cittert, 1934). The Fourier transform of the visibilities yields the brightness distribution of the light produced by the observed area of the sky (with some caveats of course). This can be used to reconstruct what the sky looked like during an observation and thus create images of measured radio signals. A VLBI array has extremely long baselines compared to a "standard" interferometer, leading to extremely high attainable resolutions given by

$$\theta \sim \frac{\lambda}{B}, \tag{1.1}$$

where θ is the resolution, λ is the observing wavelength, and B the maximum baseline distance. A side-effect of these long baselines is a relatively high surface brightness requirement of temperatures above 10^5 K (Radcliffe et al., 2018). Advanced calibration techniques, such as multi-source self-calibration (MSSC), can reduce the required temperatures somewhat. However, they cannot always be applied (Radcliffe et al., 2016).

Throughout this thesis, we will use the radio interferometer measurement equation (RIME) framework to describe interferometry and the attributes and quantities

that surround it. The astronomy software suites used in this thesis are the Common Astronomy Software Applications (CASA, McMullin et al., 2007) and Astronomical Image Processing System (AIPS, Greisen, 2003) packages, along with Python and the NumPy (Oliphant, 2006; Van Der Walt, Colbert, and Varoquaux, 2011) and SciPy (Virtanen et al., 2020) Python modules. CASA and AIPS were developed by the National Radio Astronomy Observatory (NRAO). The European Southern Observatory (ESO) and the National Astronomical Observatory of Japan (NAOJ) also work on CASA.

1.1.1 The RIME

In this section, we will discuss the derivation of the RIME as a mathematical framework that can be used to understand the effects of factors such as the primary beam attenuation of antennae on the resulting data and how these effects can be mitigated or removed. We will also consider the RIME in terms of a wide FoV observation. The entire discussion here regarding the RIME will be based on the framework developed by Smirnov (2011a) and Smirnov (2011b), which builds on work by Hamaker, Bregman, and Sault (1996) and Hamaker (2000), and the in-depth description of interferometry by Thompson, Moran, and Swenson (2017).

Initially, we consider a monochromatic point source in the sky. Suppose we set up a three-dimensional (3D) Cartesian system with the z-axis pointing directly at the source from the observer's location. In that case, the complex signal it produces can be given by $\boldsymbol{e} = \binom{e_x}{e_y}$. It is also assumed that any alterations or corruptions to this signal as it travels through space and through an individual instrument act like linear transformations, which can be represented by 2×2 Jones matrices, $\boldsymbol{J_n}$, where n indicates the n-th corruption. As per linear algebraic theorems, such left-multiplied linear transformations can be given by a single matrix called the Jones chain, which is given by $\boldsymbol{J}$. The complex voltage, which is then measured by a telescope after a Jones chain has been applied to $\boldsymbol{e}$, is given by

$$\boldsymbol{v} = \begin{pmatrix} v_a \\ v_b \end{pmatrix} = \boldsymbol{J}\boldsymbol{e}, \tag{1.2}$$

where a and b label the antenna feeds, which could be linear or circular polarisation.

In the context of interferometry, we consider the voltage measurements made by two independent telescopes, given by $\boldsymbol{v}_p$ and $\boldsymbol{v}_q$, where p and q represent the telescopes. The correlator of the interferometer then determines the visibility matrix $\boldsymbol{V}_{pq} = 2\langle \boldsymbol{v}_p \boldsymbol{v}_q^H \rangle$[1], where the voltages are time- and frequency-averaged over small intervals across the mentioned domains, pq represents the baseline between antenna p and antenna q, and the H superscript indicates the complex conjugate being taken. If one assumes that the Jones matrices that make up the Jones chains are

[1] The factor of 2 added here is a matter of convention.

time-independent, then you can obtain

$$\boldsymbol{V}_{pq} = 2\boldsymbol{J}_p\langle \boldsymbol{e}\boldsymbol{e}^H\rangle \boldsymbol{J}_q^H, \tag{1.3}$$

where $\boldsymbol{J}_p$ and $\boldsymbol{J}_q$ are the Jones chain of antennae p and q respectively. The brightness matrix, $\boldsymbol{B}$ is then defined to be equal to

$$\boldsymbol{B} = 2\langle \boldsymbol{e}\boldsymbol{e}^H\rangle, \tag{1.4}$$

which leads to

$$\boldsymbol{V}_{pq} = \boldsymbol{J}_p\boldsymbol{B}\boldsymbol{J}_q^H \tag{1.5}$$

as the final equation. Equation 1.5 is then the RIME for a monochromatic point source. It may have been derived using this specific 3D Cartesian coordinate system, but it does not depend on the coordinate system used. These matrices are mathematically separate objects and choosing a different coordinate system just changes their respective representations and does not alter their relationships (Smirnov, 2011a). For a collection of point sources, Equation 1.5 changes slightly to become

$$\boldsymbol{V}_{pq} = \sum_s \boldsymbol{J}_{sp}\boldsymbol{B}_s\boldsymbol{J}_{sq}^H, \tag{1.6}$$

where s indicates the source index.

Equation 1.6 leads naturally to the continuous case, which aligns more with the real world since the sky is considered to have a continuous light distribution. However, before the continuous RIME can be described, a new coordinate system specifically for interferometry must first be introduced. Thompson, Moran, and Swenson (2017) give an in-depth description of this system and the application and implications thereof.

We define a Cartesian coordinate system with a known reference point as its origin. This reference point can be an antenna or a point in space relative to the array. The vector from the reference point to the phase reference position in the sky is given by $\boldsymbol{s_0}$. The three axes in this coordinate system are given by $\boldsymbol{u}$, $\boldsymbol{v}$, and $\boldsymbol{w}$, and are measured in wavelengths. The $\boldsymbol{w}$ axis lies on the $\boldsymbol{s_0}$ vector such that for any antenna position $\boldsymbol{u_p} = \left(u_p, v_p, w_p\right)$, we have $\boldsymbol{u_p} \cdot \boldsymbol{s_0} = w_p$. The $\boldsymbol{u}$-axis points due East, and the $\boldsymbol{v}$-axis points towards the North. The plane created by these two axes is also orthogonal to $\boldsymbol{s_0}$. A coordinate system is also created in the sky, where the celestial sphere is projected onto a plane orthogonal to $\boldsymbol{s_0}$ and whose direction cosines are given by $\boldsymbol{l}$ and $\boldsymbol{m}$, corresponding to $\boldsymbol{u}$ and $\boldsymbol{v}$, respectively. The third sky-axis, $\boldsymbol{n} = \sqrt{1 - l^2 - m^2}$, is measured with respect to $\boldsymbol{w}$. Lastly, the vector $\boldsymbol{s} = \boldsymbol{s_0} + \boldsymbol{\sigma}$ points from the $\boldsymbol{uvw}$ reference point to the point of interest in the sky plane (the plane created by $\boldsymbol{l}$ and $\boldsymbol{m}$), given by (l, m, n), where l and m are the offsets from the phase reference point in the sky, given by $\boldsymbol{\sigma}$. These coordinate systems are depicted

in Figure 1.1.

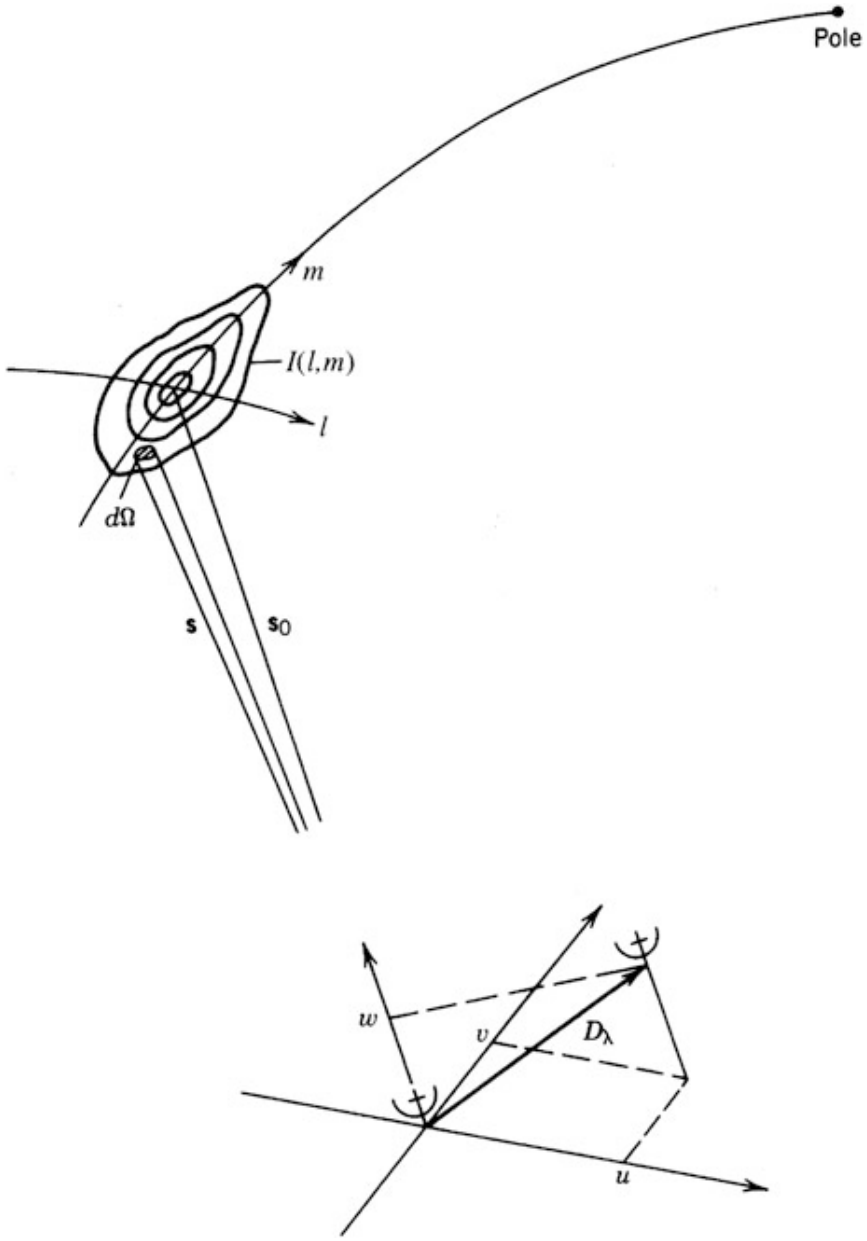

FIGURE 1.1: The coordinate system used in interferometry as defined in Section 1.1.1. Figure from Thompson, Moran, and Swenson (2017).

Returning to the RIME, each Jones matrix can be split into three major components to be $\boldsymbol{J}_p = \boldsymbol{G}_p\boldsymbol{E}_p\boldsymbol{K}_p$, where $\boldsymbol{G}_p$ denotes the direction-independent effects (DIEs), $\boldsymbol{E}_p$ the direction-dependent effects (DDEs), and $\boldsymbol{K}_p$ is the scalar phase matrix (Smirnov, 2011a). $\boldsymbol{K}_p$ is the simplest of these three. It is given by

$$\boldsymbol{K}_p = \exp\left(-2\pi i \boldsymbol{u_p} \cdot \boldsymbol{s}\right) \mathbf{I}_{2\times 2} \tag{1.7}$$

$$= \exp\left\{-2\pi i \left[u_p l + v_p m + w_p (n-1)\right]\right\} \mathbf{I}_{2\times 2}. \tag{1.8}$$

$\boldsymbol{G}_p$ and $\boldsymbol{E}_p$ are more intricate than $\boldsymbol{K}_p$. These can be seen as Jones matrices in their

own right, as they contain all of the relevant corruptions applied to the signal as it travels through space and the instrument. Generally speaking, both $\boldsymbol{G}_p$ and $\boldsymbol{E}_p$ are functions of time, but only $\boldsymbol{E}_p$ is a function of l and m. The RIME, as given by Equation 1.6, can be rewritten to become

$$\boldsymbol{V}_{pq} = \boldsymbol{G}_p \left(\sum_s \boldsymbol{E}_{sp} \boldsymbol{K}_{sp} \boldsymbol{B}_s \boldsymbol{K}_{sq}^H \boldsymbol{E}_{sq}^H \right) \boldsymbol{G}_q^H. \tag{1.9}$$

The integral version of this equation is

$$\boldsymbol{V}_{pq} = \boldsymbol{G}_p \left(\iint_{lm} \frac{1}{n} \boldsymbol{E}_p \boldsymbol{B} \boldsymbol{E}_q^H e^{-2\pi i \left[u_{pq} l + v_{pq} m + w_{pq} (n-1) \right]} \mathrm{d}l \mathrm{d}m \right) \boldsymbol{G}_q^H, \tag{1.10}$$

where $\boldsymbol{u}_p - \boldsymbol{u}_q = \boldsymbol{u}_{pq} = \left(u_{pq}, v_{pq}, w_{pq} \right)$.

Equation 1.10 is incredibly close to representing a pure Fourier transform relationship between $\boldsymbol{V}_{pq}(u,v)$ and $\boldsymbol{B}(l,m)$. Steps can be taken to make this the case. Firstly, the bounds of the integrals can be set to $-\infty$ and ∞ because the primary beams of the antennae will force the integrand to zero (Thompson, Moran, and Swenson, 2017). Secondly, the integral can be changed into a 3D Fourier transform or a 2D one. The 2D case is simpler to deal with and is also the conventional form of the RIME, so it will be described here (for a detailed look into the 3D case, see Perley (1999)). For this equation to be considered a 2D Fourier transform, the $w_{pq}(n-1)$ term must be neutralised.

There are a few ways to accomplish this. This automatically happens if l and m are small (i.e. small observation FoV or data close to phase centre). Alternatively, if this term approaches 1, algorithms like W-Projection can project the visibilities to $w = 0$ and deconvolve the effects of the non-coplanarity of the baseline (Cornwell, Golap, and Bhatnagar, 2005). Another way of approaching this problem is by deriving calibration tables that can divide out the w_{pq} terms (Smirnov, 2011a). This can be done by splitting the w_{pq} term and, subsequently, the exponential into separate terms for the individual antennae. Doing so results in $\boldsymbol{W}_p = \frac{1}{\sqrt{n}} e^{-2\pi i w_p (n-1)} \mathbf{I}_{2\times 2}$ for any antenna p (in the RIME you get $\boldsymbol{W}_p$ and $\boldsymbol{W}_q^H$). Since the $\boldsymbol{W}_p$ matrices are examples of DDEs, they can be absorbed into the $\boldsymbol{E}_p$ Jones matrix in the RIME, which represents all such effects.

This then leads to a 2D Fourier transform relationship between $\boldsymbol{V}_{pq}$ and $\boldsymbol{B}$ given by

$$\boldsymbol{V}_{pq} = \boldsymbol{G}_p \left(\iint_{lm} \boldsymbol{B}_{pq} e^{-2\pi i \left[u_{pq} l + v_{pq} m \right]} \mathrm{d}l \mathrm{d}m \right) \boldsymbol{G}_q^H, \tag{1.11}$$

where $\boldsymbol{B}_{pq} \equiv \boldsymbol{E}_p \boldsymbol{B} \boldsymbol{E}_q^H$ is the so-called "apparent sky" as seen by the baseline created between antennae p and q and the $\frac{1}{n}$ factor was absorbed into the DDE matrices. This equation is the final form of the RIME. In Chapter 2, the primary beams of the antennae and their relationship with the RIME will be discussed further.

1.1.2 Why VLBI?

In this section, we aim to explain why VLBI is useful for astronomy and why it is worth developing the technique further. We will do this by highlighting work done with VLBI arrays, which serve as examples of VLBI's capability to unlock information in the sky.

The most well-known VLBI result in the history of the field by far is the image of the supermassive black hole (SMBH), M87*, made with the Event Horizon Telescope (EHT, Event Horizon Telescope Collaboration et al., 2019). The results obtained by the EHT confirmed theoretical predictions made by Einstein (1915) in his theory of general relativity and, in effect, proved the existence of black holes beyond a doubt. This study also provided a unique insight into AGN models' accuracy in general-relativistic magnetohydrodynamic (GRMHD) simulations. The EHT results from nearly a decade's worth of technical and infrastructure upgrades to existing antennae, which when coupled with the extremely fine resolution of $\sim 25\ \mu$as reached due to the long baselines, shows the power of VLBI in the modern landscape. More recently, the EHT managed to image the event horizon of the SMBH in the centre of the Milky Way, Sagittarius A* (Event Horizon Telescope Collaboration et al., 2022). Both of these observations required the development of new calibration and observation techniques, which undoubtedly will be useful in future observations.

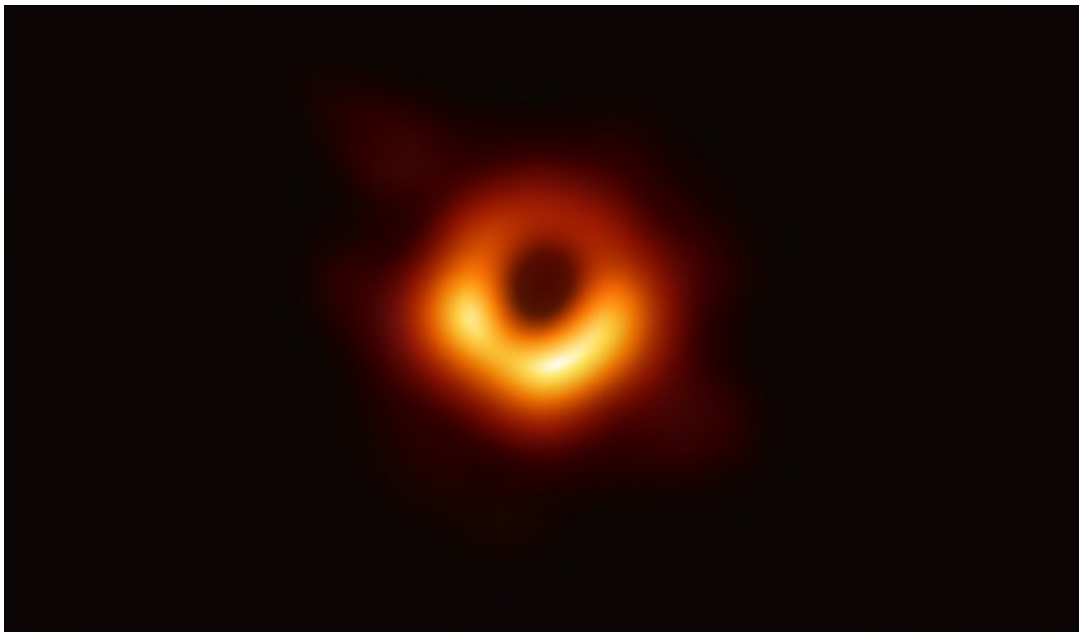

FIGURE 1.2: VLBI image of the SMBH M87*. Credit to Event Horizon Telescope Collaboration et al. (2019).

Surveys have been conducted to determine the science prospects of the Square Kilometre Array (SKA) once it becomes operational. One such survey is SPARCS, a collection of surveys done to pre-empt the sources the SKA will be able to observe.

Njeri et al. (2022) combined the EVN and *e*-MERLIN arrays to conduct a VLBI survey of the SPARCS-North field with wide-field observations. The combination of the EVN and *e*-MERLIN leads to a mix of short and long baselines, thus unlocking the ability to observe large- and small-scale structures in a single session. Including VLBI in such surveys allows for the detection of bright, compact sources in combination with the broader emission seen by traditional interferometers such as the *e*-MERLIN. This allows for AGN activity to be effectively separated from star formation activity since VLBI has a relatively high surface brightness requirement, which distant star-forming regions do not meet (Radcliffe et al., 2018). VLBI is thus important in the context of the cosmology done via the SKA and in determining science targets for the interferometer.

One of the strong advantages of the wavelengths wherein VLBI observations are conducted is that they are impervious to dust surrounding AGN. This allows traditional interferometry to observe large-scale structures surrounding typical AGN, such as jets (occasionally, VLBI also detects jets). The additional sensitivity requirements associated with VLBI result in the compact, central source still visible to a VLBI array even when obscured. Because of this, many VLBI observations have been conducted to search for them. While the VLBI AGN detection rate is lower than other regimes, such as X-ray observations, improvements in array sensitivities will undoubtedly increase the effectiveness of VLBI in detecting AGN, especially obscured AGN (Middelberg et al., 2011). Examples of such VLBI studies where AGN were the main targets are Radcliffe et al. (2018), Middelberg et al. (2011), Middelberg et al. (2013), and Chi, Barthel, and Garrett (2013).

As mentioned before, the high surface temperature requirement causes VLBI to be ideal for AGN detection, which is reflected in the papers published that made use of the EVN (Venturi et al., 2020). VLBI studies are largely focused on AGN detection and developing multi-wavelength models of these phenomena, such as Radcliffe et al. (2018) and Radcliffe et al. (2021) and Njeri et al. (2022). In more recent years, especially as the field of wide-field observations grew, VLBI found use in different fields. Examples of this are gravitational lensing studies such as Spingola et al. (2018), Spingola et al. (2019), and the ISM distribution work done by Morgan et al. (2013). The more recently discovered phenomenon of FRBs has also been investigated in the context of VLBI (Leung et al., 2024). FRBs are luminous bursts of light in the radio spectrum that only last mere milliseconds. FRBs also have small angular dimensions, which makes wide-field VLBI observations ideal for finding them. Some FRBs have been localised using VLBI, which allowed for their origins to be found (Marcote et al., 2017; Marcote et al., 2020; Kirsten et al., 2022; Nimmo et al., 2022). Supernova remnants are also studied using VLBI, as the high resolution allows for a detailed image to be obtained of such bright objects. One such example is the observation of supernova remnant SNR 4449-1 by Mezcua, Lobanov, and Martí-Vidal (2013) using the EVN. These are only some of the applications of VLBI. It truly is a

valuable asset to the astronomy field as a whole.

1.2 AGN

AGN are incredibly luminous celestial objects associated with the accretion activity of SMBHs at the centres of galaxies (Heckman and Best, 2014; Padovani et al., 2017). They are considered to be the brightest non-explosive celestial objects to exist. They tend to be luminous across the electromagnetic spectrum and are thus a major point of multi-wavelength astronomical study (Padovani et al., 2017). This led to various labels being associated with them being collectively referred to as the AGN zoo, as the individual wavelength communities studying them were somewhat disjointed. Traditional labels include quasi-stellar objects (QSOs), quasars, blazars, low-ionization nuclear emission-line regions (LINERs), radio-loud and radio-quiet galaxies, etc.

More relevant and less ambiguous labels in the modern era of astronomy are jet-mode and radiative-mode AGN (Heckman and Best, 2014), which line up with models of AGN derived from their observed multi-wavelength characteristics. The aforementioned models of AGN fall under the unification models of AGN, which attempt to describe the characteristics of such objects observed across the electromagnetic spectrum using a single physical model (Bianchi, Maiolino, and Risaliti, 2012; Heckman and Best, 2014; Netzer, 2015). These models still have some problems that must be addressed, but generally match observational data.

Another aspect of AGN, which is only a somewhat recent revelation, is their impact on the evolution of their host galaxies. Relationships have been established between the statistical properties of the central SMBH and properties of their host galaxies, such as the galactic star formation rate and growth rate of the SMBH (Heckman and Best, 2014). Relationships such as this fall under AGN feedback, where the AGN and its host galaxy influence each other in a feedback loop, which leads to phases of AGN activity and phases of star formation throughout the lives of galaxies. The exact mechanisms are still debatable, although some theories have been developed (Silk, Di Cintio, and Dvorkin, 2014). This means that wide-field VLBI AGN studies and surveys have impacts on cosmology since AGN are seemingly so connected to the evolution of the universe.

AGN are a major focal point of VLBI studies since they are bright and compact objects in the sky, which is ideal for VLBI observation. Countless VLBI surveys have been conducted in the past, specifically searching for AGN and relationships between VLBI detections and other wavelengths such as the X-ray, infrared, and optical regimes. Traditionally, VLBI struggled to attain a high detection rate of known AGN, which largely was due to historically low sensitivities (Middelberg et al., 2011). With new technology, correlation and calibration techniques and wide-field observations, the aim is to improve this detection rate.

1.3 Wide-field observations

Interferometric equations such as the RIME are derived in the context of monochromatic sources, receivers, and single moments in time. Because of this, the observational data used to create the visibilities are averaged into single frequency channels and time steps. Due to technological constraints in earlier years, the frequency channels and time steps over which the data were averaged were large. This led to the main limitations on the FoVs of VLBI observations being bandwidth and time smearing (Garrett et al., 1999). Upgrades to underlying VLBI systems and individual array elements gradually lifted these constraints, but they slowed down drastically in the 1980s. To showcase the small FoV generally obtained, we can consider a typical EVN observation done in the 1990s. At a central observing wavelength of 18 cm, the resulting FoV of the observation would have been a meagre ~ 0.5 arcmin, which does not even reach 10% of the width of the Effelsberg telescope, which is by far the telescope with the smallest FoV in the EVN today.

Bandwidth smearing occurs when the data are averaged over too wide frequency channels, resulting in radially broadened sources when imaged in continuum observations (Thompson, Moran, and Swenson, 2017). This type of smearing is analogous to chromatic aberration in optical systems (Middelberg and Bach, 2008). Time smearing occurs when the time steps over which the data are correlated and averaged are too long. It happens because the rotation of the Earth does not get accounted for across single time steps. Time smearing is similar in appearance when imaging to bandwidth smearing, but it occurs orthogonal to bandwidth smearing and is thus circumferential instead of radial. Time smearing also decreases the peaks of the baselines' responses, reducing the array's sensitivity. These types of smearing can be reduced by decreasing the width of the averaged element. For bandwidth smearing, finer frequency channels should be used, and smaller time steps should be implemented for time smearing. This has the caveat of leading to larger datasets and taking longer to calibrate.

Modern VLBI arrays have upgraded computational capabilities, storage systems, and software correlators (Deller et al., 2007; Deller et al., 2011), which allow for small enough frequency channels and time-averaging steps such that smearing due to them is no longer an FoV-reducing factor. Using these modern software correlators, multiple phase centres can be set in a single observation, substantially increasing the available observation FoV (Morgan et al., 2013). When software correlators are combined with algorithms like multi-source self-calibration (MSSC, Radcliffe et al., 2016), or when a large amount of phase centres are used, smearing can be eliminated. This leaves only the attenuation caused by the primary beams of the array elements to be dealt with for wide-field observations to become the norm, as Garrett et al. (1999) predicted.

The prospect of wide-field VLBI observations has been tested periodically on the

EVN throughout the past, as evident in Garrett et al. (1999), Garrett et al. (2001), Garrett, Wrobel, and Morganti (2005), and Chi, Barthel, and Garrett (2013), to name only a few. The obtained observation FoVs and accompanying detections gradually improved as technical upgrades were done to the arrays, culminating in the capabilities of the modern VLBI era, as Njeri et al. (2022) and Radcliffe et al. (2018) illustrate (also see Venturi et al., 2020). With regards to the Very Long Baseline Array (VLBA), Middelberg et al. (2011) showed in 2011 already that the network had reached a point technologically where accurate primary beam models could be derived and the FoVs of observations expanded substantially.

1.3.1 AGN detection and surveys

The question of why wide-field VLBI observations are important enough to be continually tested and developed throughout the years can be raised. Thus, the remainder of this section will answer this question by highlighting some results from this type of observation. Middelberg et al. (2013), Radcliffe et al. (2018), and Njeri et al. (2022) are all examples of VLBI surveys with wide-field observations of areas previously surveyed with other wavelengths and telescopes. These serve as indicators of VLBI source detection rates compared to other wavelengths. Radcliffe et al. (2018) observed the GOODS-N fields, which initially were observed by the Hubble Space Telescope (HST), using multiple pointings, each with a radius of 7.5′, and found 31 faint VLBI sources. Their findings build upon the findings of Garrett et al. (2001) and Chi, Barthel, and Garrett (2013), further showcasing the development of the underlying technology of the EVN and *e*-MERLIN, which ultimately improved the prospects of wide-field VLBI observations. Njeri et al. (2022) also conducted a wide-field observation using the EVN combined with the *e*-MERLIN. They observed the Northern regions of the area covered by the SPARCS survey and detected 11 sources with microarcsecond resolutions. Additionally, they may have found a resolution boundary between AGN activity and star formation. Both Radcliffe et al. (2018) and Njeri et al. (2022) used estimated primary beam models and the multiple phase centre technique to expand the FoVs of their observations.

Middelberg et al. (2013) conducted a study of the Lockman Hole using the VLBA and a series of wide-field observations stitched together in a technique called "mosaicking". They expanded the FoV of each epoch by applying models of the primary beams derived by Middelberg et al. (2011). They detected 65 sources from 217 radio sources. The authors also indicate that their study may have found a possible correlation between star formation and AGN activity. All three works show the versatility and applicability of wide-field observations in the modern VLBI landscape and highlight possible detections that would be made. When combined with software correlators using the multiple phase centre technique, MSSC, and accurate primary beam models, the FoVs of VLBI observations can be expanded substantially. This

opens the possibility of conducting high-resolution and high-sensitivity sky surveys in a timely fashion - which was only dreamt of 20 years ago.

1.3.2 Other applications of wide-field observations

Taking a step away from purely searching for AGN allows for many other applications of wide-field VLBI observations. Morgan et al. (2013) is an excellent example of a wide-field VLBI observation using the VLBA to study the background of a local galaxy, M31, and to see if the results could be used to derive information about the distribution of ionised ISM throughout the galaxy. Out of 200 sources observed simultaneously (thanks to modern software correlation), 16 were detected and classified by the authors as AGN. All of these AGN were detected as background objects behind the galaxy. The widths of the detected AGN were measured and compared with sizes typically expected, and the conclusion was drawn that scattering-induced broadening of the detected AGN was taking place - thus proving that wide-field VLBI observations could be used for ionised ISM density studies in local galaxies. Figure 1.3 showcases the area of M31 that was expected to be observed in the single wide-field VLBA observation.

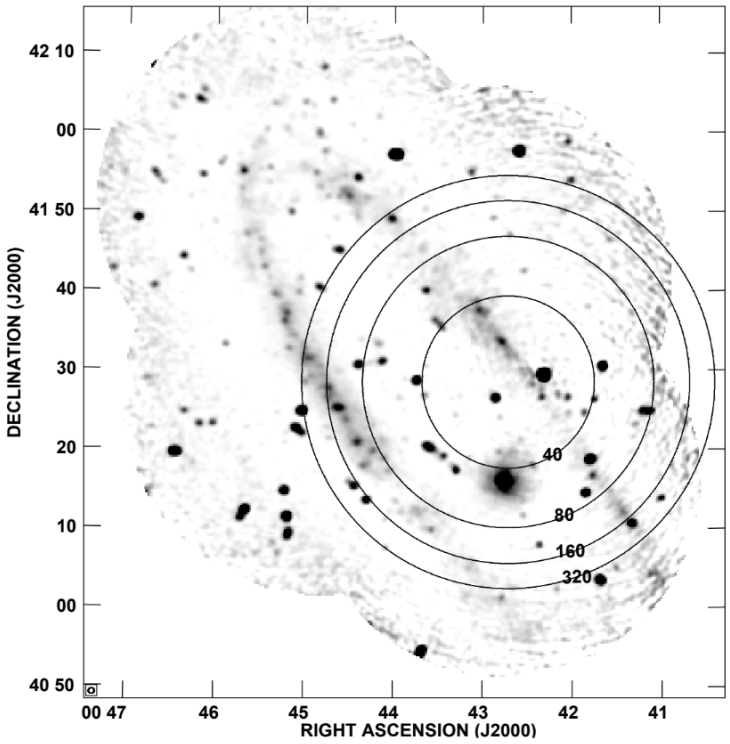

FIGURE 1.3: Karl G. Jansky Very Large Array (JVLA) image of M31 with expected root mean square sensitivities (μJy/beam) overlayed as the circular contours. This image depicts the size of the area observed during a wide-field observation conducted using the VLBA. Sourced from Morgan et al. (2013)

Spingola et al. (2019) is another example of where wide-field VLBI observations can be used. Gravitational lensing occurs when a source's light passes through an area with a large mass distribution and then becomes distorted as a result. It typically occurs with galaxies and galaxy clusters (Spingola et al., 2019). If the lensing mass reaches a critical mass, then multiple images are created of the source object. The resulting images resulting from lenses typically are ring-like structures - the diameter of which depends on the lens mass. Gravitational lenses can also be used to determine the mass distribution of the area within the ring and allow one to determine the limits of lens mass. This can be used to determine the masses of SMBHs, for instance, and can also be used to estimate the distribution of dark matter (Spingola, 2022). This phenomenon can also be used as a tool to calculate cosmological parameters such as the Hubble constant. These lenses also magnify their background, which allows for the imaging of distant invisible redshifted regions of the Universe. Thus, the study of gravitational lensing is an incredible tool that allows for many aspects of the Universe to be studied.

The mJy Imaging VLBA Exploration at 20 cm (mJIVE-20, Deller and Middelberg, 2014) is an extremely comprehensive VLBI survey conducted on the VLBA. At the time of Spingola et al. (2019)'s publication, it had detected 4965 sources. Spingola et al. (2019) filtered the mJIVE-20 results in search of lensing candidates and subsequently observed them at high resolutions using the VLBA, where they had 12 lensing candidates. They detected two known lenses directly from the wide-field mJIVE-20 survey data (without a follow-up VLBA observation), bringing the total up to 14. Their work shows that wide-field VLBI surveys would invariably lead to the detection of gravitationally lensed objects and that they could be found using the right set of selection criteria. Furthermore, they believe that a VLBA survey with a sensitivity of 140 μJy/beam over an area of 9.42 steradian should detect roughly 530 gravitationally lensed objects.

The exact origins of FRBs are a major point of research presently and VLBI is in the ideal position to be at the forefront of this field (Marcote et al., 2017; Marcote et al., 2020). FRBs are extremely localised and require exact knowledge of their position for follow-up observations to be done and their causes to be found. VLBI offers the resolution for this to be done, but it lacks the FoV. Wide-field VLBI takes this one step further by allowing for large areas of the sky to be observed at the same time - thus increasing the area wherein FRBs can be detected at any one time (Venturi et al., 2020). VLBI arrays such as the EVN can work in combination with instruments like the Canadian Hydrogen Intensity Mapping Experiment (CHIME) to detect and localise FRBs. The development of FRB science has major implications for the whole astronomy field. Firstly, it will force VLBI arrays to improve their technology and techniques further to be able to detect them (Venturi et al., 2020). Secondly, FRBs are thought to be able to be used for a multitude of scientific discoveries, such as high-energy astrophysical phenomena, the probing of baryonic matter distribution

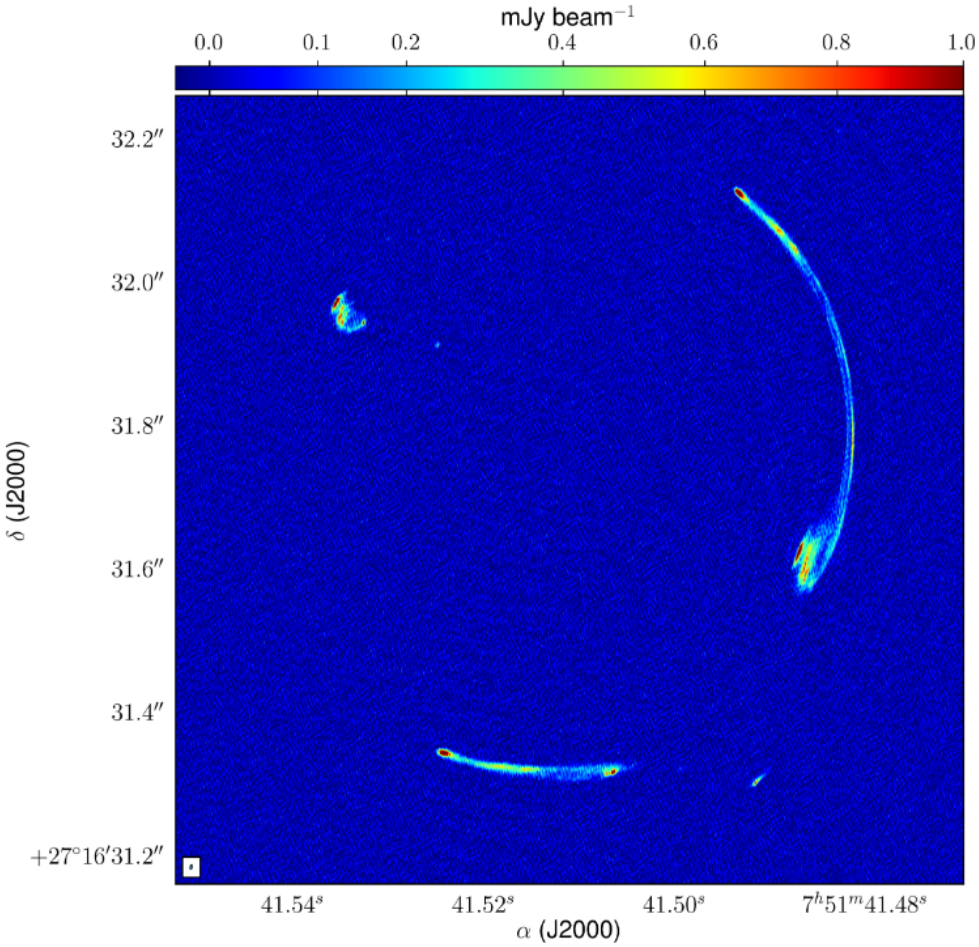

FIGURE 1.4: A global VLBI (EVN+VLBA) image of MG J0751+2716. The label δ represents declination and α right ascension. Comprehensive wide-field high-resolution and high-sensitivity VLBI surveys will allow for the detection of many more sources such as these, as the current lack of VLBI survey sky-coverage hinders this field of study. Figure from Spingola et al. (2018).

in the Universe, and the dark energy equation-of-state parameter (Marcote et al., 2017; Venturi et al., 2020; Zhou et al., 2014).

It should be clear at this point that wide-field VLBI observations have the potential to unlock many new results in the whole field of astronomy and effort should therefore be undertaken to improve the VLBI arrays to allow them to perform such observations reliably. In terms of the EVN, the main hindrance currently is the lack of empirical and accurate primary beam models. This thesis hopes to provide some of those models. A much more broader and in-depth discussion of the expectations of wide-field VLBI can be found in Venturi et al. (2020).

Chapter 2

The Primary Beam

In this thesis, we are interested only in aperture antennas, which reflect incoming light wavefronts into a feed containing dipoles to be measured. Because these antennas act as apertures, they are subject to Fraunhofer diffraction (Thompson, Moran, and Swenson, 2017). Furthermore, we assume all antennas are perfectly illuminated parabolic antennas with no deformation or tapering and thus act as circular apertures on incoming light waves. Additionally, we will follow the notation of Napier (1999), albeit with slight differences.

2.1 Theory

An antenna can be described in the context of radio astronomy as a device that converts electromagnetic energy into electronic signals (Condon and Ransom, 2016). The complex voltage response pattern of an antenna describes the area wherein the antenna can measure voltages based on where it is pointed. It can be derived using the van Cittert-Zernicke theorem (van Cittert, 1934; Zernike, 1938), as described by Thompson, Moran, and Swenson (2017). If we consider an antenna with a complex antenna illumination pattern of light reflected from the aperture into the feed of the antenna, given by $f(u, v)$, where the aperture lies in the uv plane, then we have that the complex voltage radiation pattern is given by

$$F(l, m) = \iint_{\text{Aperture}} f(u, v) e^{2\pi i(ul+vm)} \mathrm{d}u\mathrm{d}v, \tag{2.1}$$

where $u = \sin\theta\cos\phi$ and $v = \sin\theta\sin\phi$ are the direction cosines of the uv-plane scaled to the observing wavelength, λ, and l and m are the direction cosines of the lm plane wherein the source lies (Napier, 1999; Condon and Ransom, 2016; Thompson, Moran, and Swenson, 2017). The respective axes were chosen purposely to showcase how similar the relationship between $F(l, m)$ and $f(u, v)$ is to the relationship between $\boldsymbol{V}_{pq}$ and $\boldsymbol{B}_{pq}$ in Equation 1.10. This relationship only holds if the source distance from the antenna is greater than $\approx \frac{2D^2}{\lambda}$, where D is the antenna diameter (Condon and Ransom, 2016). Figure 2.1 shows some examples in one dimension (1D) of the resulting $F(l)$ functions for different tapering equations. The primary

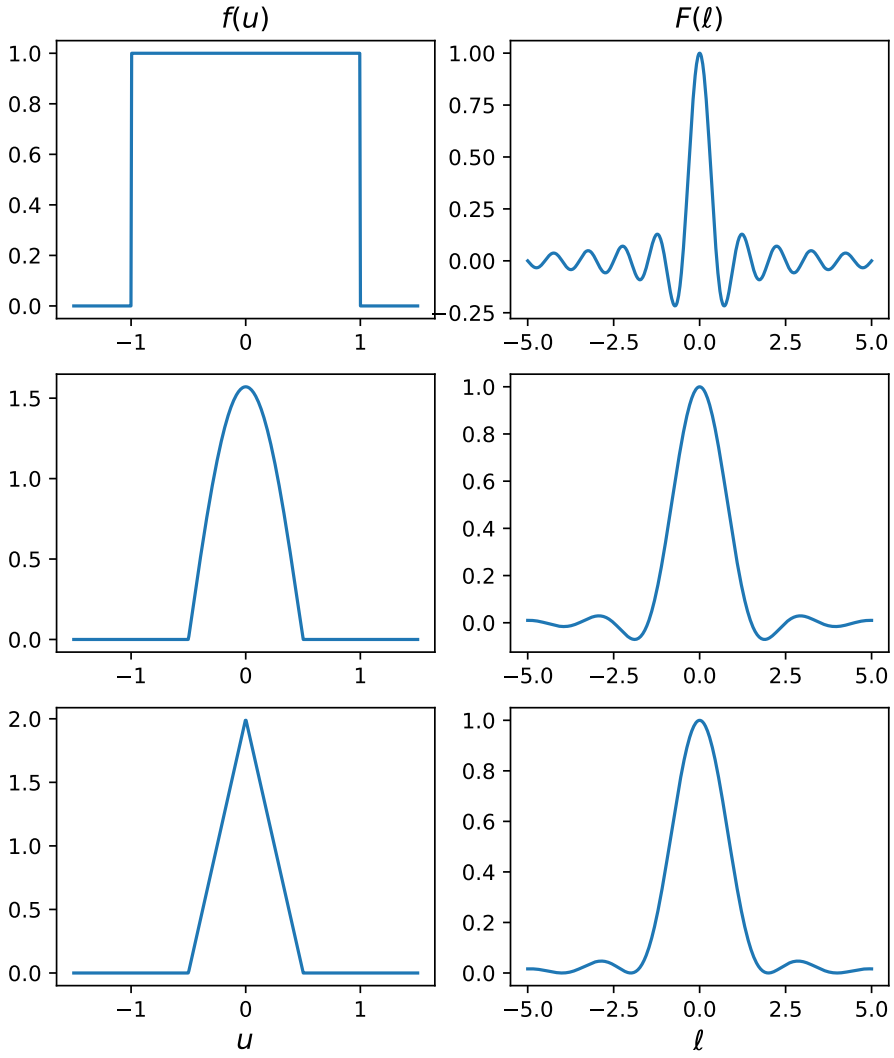

FIGURE 2.1: A selection of $f(u)$ and their resulting $F(l)$ functions.

beam can be identified in this figure as the region of the response pattern within the first nulls. The rest of the response pattern is then collectively referred to in this thesis as the sidelobes. In this figure, it can then be seen that tapering tends to reduce the sidelobes and broaden the primary beam of an antenna. Another beam-related parameter is the half-power beamwidth (HPBW), also called the full-width at half-maximum (FHWM), which is the diameter of the power pattern when it reaches half its peak measured power.

The power pattern of the antenna is then the area wherein the antenna can measure energy and its own radiated energy can be measured. It is given by

$$P(l,m) = |F(l,m)|^2 = F(l,m) \times F^*(l,m), \tag{2.2}$$

which is showcased in Figure 2.2 for a circular aperture with no tapering and uniform illumination in both 1D and 2D. Effort is usually undertaken to reduce the sidelobes as much as possible as they are considered unwanted noise (Popping, A. and Braun, R., 2008). In this thesis, we aim to model the primary beams in the power patterns of the antennas.

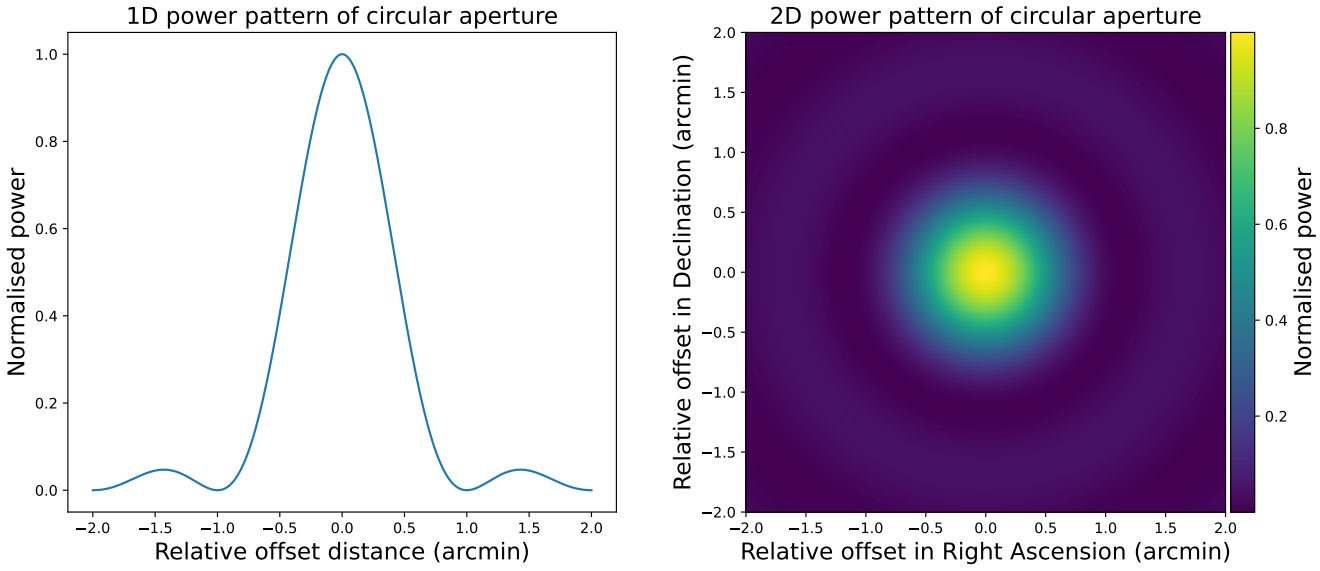

FIGURE 2.2: 1D and 2D versions of the power pattern of a uniformly illuminated circular aperture

2.1.1 Heterogeneous versus homogeneous arrays

Some arrays, such as the VLBA, consist of antennas designed to the same specifications. This means their underlying electronics, feed offsets, tapering, etc. all are designed to be the same. Such an array is called a homogeneous array. Other arrays, such as the EVN and *e*-MERLIN, consist of antennas that were designed according to different specifications. This could for instance be antennas originally designed to conduct single-antenna observations or different homogeneous arrays that are combined to form a larger array. This type of array is a heterogeneous array (Thyagarajan et al., 2017). There of course are multiple definitions of homogeneous and heterogeneous arrays, but other definitions (see Holdaway and Helfer, 1999; Hamaker, 2000) tend to ignore the contribution of factors other than antenna diameters and feeds to the shapes of their primary beams.

Each type of array has its advantages and disadvantages. The primary beams of a homogeneous array are *approximately* identical, meaning a single primary beam model can be derived and applied to all of the antennas (Middelberg et al., 2011, for instance). This makes the assumption of $\boldsymbol{E}_p(l,m) = \boldsymbol{E}(l,m)$ possible in the RIME

(Smirnov, 2011b, in this case $\boldsymbol{E}(l,m)$ represents the primary beam) and thus makes it easier to account for. In a heterogeneous array, the primary beams are vastly different due to the different diameters, tapering, feed offsets, etc. present in the system. This complicates imaging and data calibration (Thyagarajan et al., 2017). These arrays are also more flexible than homogeneous arrays in terms of observation resolution, sensitivity and baseline count. antennas with larger diameters can be added to heterogeneous arrays to have baselines with high sensitivity (but reduced FoV). Superior resolutions can be achieved by adding antennas to the network that lead to longer baselines (at the cost of higher source brightness requirements). Homogeneous arrays are not necessarily this flexible, but accounting for antenna-related effects is easier in their case.

Another complexity introduced by heterogeneous arrays is the changing of Equation 2.2 to become

$$P_{pq}(l,m) = F_p(l,m) \times F_q^*(l,m), \tag{2.3}$$

where pq is the baseline created by antennas p and q (Strom, 2004). Equation 2.3 reduces to Equation 2.2 when the antennas are homogeneous. This equation describes the baseline response, where the voltage radiation patterns of the two antennas are combined.

This combination of antenna responses has interesting consequences. When large antennas, such as the 100 m Effelsberg radio telescope, are combined with a more commonly sized antenna (25 m or 32 m), the FoV of the larger telescope can be widened substantially (Strom, 2004). Figure 2.3 shows the effect of this combination on the HPBW of the larger antenna.

2.1.2 Primary beam equations

The normalised power pattern of a perfectly illuminated one-dimensional antenna without tapering is axisymmetric (Thompson, Moran, and Swenson, 2017) and is given by

$$P(\theta) = \mathrm{sinc}^2\left(\frac{D\theta}{\lambda}\right), \tag{2.4}$$

where $D/\lambda \gg 1$, D is the antenna diameter, λ the observing wavelength and $\theta = \sqrt{l^2+m^2}$ is the offset from the pointing centre (Condon and Ransom, 2016). The general formula for the HPBW is

$$\theta_{\mathrm{HPBW}} = K\frac{\lambda}{D}, \tag{2.5}$$

where K is a scaling factor. The scaling factor has numerous reported values and depends on the tapering and real power pattern of each antenna, so it is nearly impossible to really generalise its value. According to Condon and Ransom (2016), the analytical value for K is 0.89, Napier (1999) has it as 1.02, and Morgan et al.

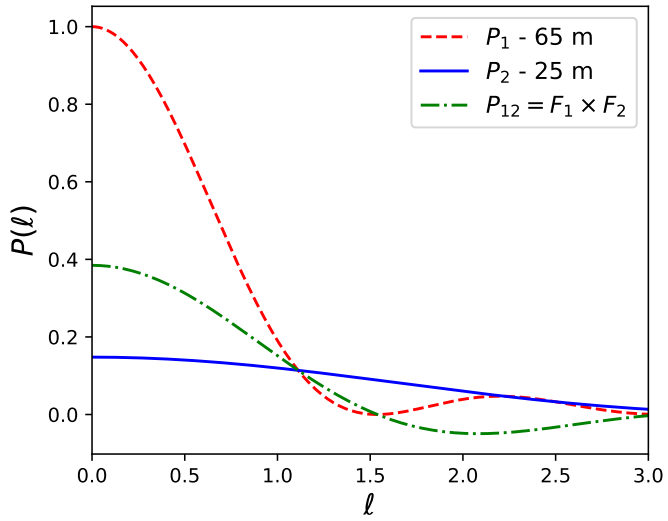

(A) Power patterns of 65 m and 25 m parabolic untapered antennas and their resulting baseline response. The latter two are scaled by the normalized sensitivity of the 65 m antenna.

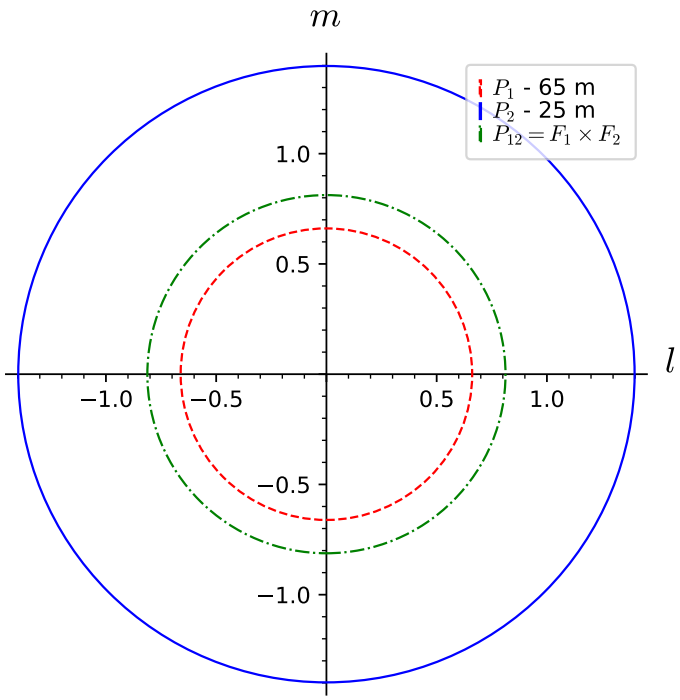

(B) The HPBWs of the antenna responses in 2.3a are shown from a top-down view of the lm plane.

FIGURE 2.3: The effects of combining antennas with different primary beams on the resulting baseline response pattern.

(2011) reports it as 1.2 for Gaussian beams. In this thesis, we will assume a value of 1 for K. The reasoning behind this is made clear in Chapter 6 but can be summarised as allowing different levels and types of tapering of the different antennas to be present and accounted for. Cosine tapering such as the second row in Figure 2.1 is an improved approximation of the real-world illumination patterns usually

obtained (Condon and Ransom, 2016). This leads to a power pattern of

$$P(\theta) = \left[\frac{\cos\left(\pi\theta D/\lambda\right)}{1-4\left(\theta D/\lambda\right)^2}\right]^2, \tag{2.6}$$

which has an analytical

$$\theta_{\text{HPBW}} \approx 1.2\frac{\lambda}{D}. \tag{2.7}$$

There are of course other tapering schemes used. The antennas in the Westerbork Synthesis Radio Telescope (WSRT), for instance, are 25 m parabolic antennas whose primary beams are given in the GHz regime by $\cos^6\left(68\nu\theta\right)$, where ν is the observing frequency and θ the radial offset from the FoV centre in degrees (Popping, A. and Braun, R., 2008).

Finally, if we assume that $\boldsymbol{E}_p$ is a DDE which represents the power pattern of antenna p in the RIME, then we have that

$$\boldsymbol{E}_p = \begin{pmatrix} \sqrt{P_p} & 0 \\ 0 & \sqrt{P_p} \end{pmatrix}. \tag{2.8}$$

Equation 2.8 reveals a subtle assumption made in this thesis: we assume that beam squint does not exist (i.e. that E_p is a scalar matrix). Beam squint occurs when the receptors in an antenna's feed are misaligned, meaning their respective response patterns are also misaligned (Uson, Juan M. and Cotton, W. D., 2008). It also occurs when the feed of the antenna is offset by an angle with respect to the reflector's central axis. For antennas with Alt-Azimuth mounts, this also becomes a time-dependent problem as the parallactic angle of the sky changes as the observation is conducted. Beam squint is not impossible to correct for and is not too intricate to model, but it is not in the scope of this thesis. Here we assume that the feeds of the antennas are not offset from the reflector axis and that the receptors are not misaligned. These assumptions make $\boldsymbol{E}_p$ a time-independent scalar matrix, i.e $\boldsymbol{E}_p(t,l,m) = \mathrm{E}_p(l,m)$. In terms of the RIME, the apparent brightness then becomes

$$\boldsymbol{B}_{pq} = \mathrm{E}_p\mathrm{E}_q\boldsymbol{B} = \mathrm{E}_{pq}\boldsymbol{B}, \tag{2.9}$$

where E_{pq} is simply the product of $\mathrm{E}_p\mathrm{E}_q$.

2.2 Modelling of the primary beam

There are various ways of modelling the primary beam. This includes a sinc^2 function, a Gaussian distribution (Middelberg et al., 2013; Radcliffe et al., 2018), a Jinc function (Uson, Juan M. and Cotton, W. D., 2008) or even a polynomial such as with the WSRT (Popping, A. and Braun, R., 2008). These models, however, can only be

used to model the primary beam and not the entire power pattern. The real antennas start deviating from the ideal case typically beyond the HPBW of the antenna. In the case of the Gaussian, an additional reason is that the model is not in any way periodic such as the sinc^2 and Jinc functions are. Thus, the Gaussian model cannot account for any sidelobes. The advantage of the periodic sinc^2 and Jinc functions is lost, however, as they assume a simple sidelobe structure and cannot replicate the intricate real-world sidelobes (again, beyond the HPBW asymmetries in the power pattern can become visible). Figure 2.4 shows a comparison between a standard sinc^2 function and a Gaussian distribution fitted ($b = 0.365$ rad) to it. The conclusion to be drawn from this figure is that the Gaussian distribution is a suitable model for the primary beam within the HPBW, which further validates the use of a Gaussian model in this thesis.

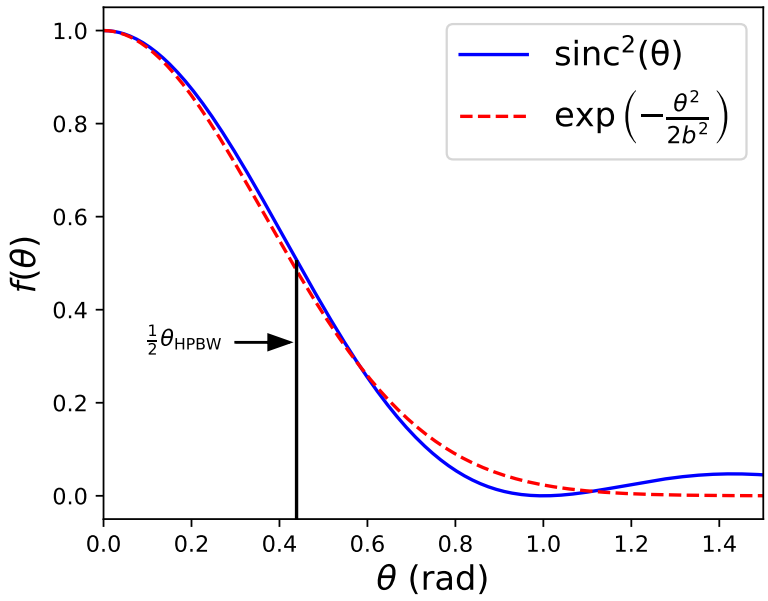

FIGURE 2.4: A Gaussian distribution fitted to a sinc^2 function.

The Gaussian distribution model will be used in this thesis to model the primary beams of the EVN and *e*-MERLIN antennas. The model is given by

$$P(\theta) = a\text{exp}\left(-\frac{\theta^2}{2b^2}\right), \tag{2.10}$$

where a and b are fit-parameters. If the data used to generate fits are normalised, a is set to one and essentially eliminated. This model type assumes tapering is present in the antenna, which is ideal for a heterogeneous array since the antennas were mostly

originally designed for solo operation, which means most antennas have some tapering. Equation 2.10 can be expanded to any wavelength by using the equation

$$P(\theta)_{p,\nu} = \exp\left(-\frac{4\ln(2)D_{p,\text{eff}}^2\theta^2}{\lambda^2}\right), \tag{2.11}$$

where ν is the frequency corresponding to the wavelength λ, and $D_{p,\text{eff}}$ is the effective diameter for the model representing antenna p. The effective diameter is given by

$$D_{p,\text{eff}} = \frac{\lambda}{2\sqrt{2\ln(2)}b_p}, \tag{2.12}$$

where b_p is the fit-parameter for the model of antenna p.

The HPBW of the Gaussian distribution is given by

$$\theta_{\text{HPBW}} = 2\sqrt{2\ln 2}b, \tag{2.13}$$

which can be used to determine the model diameter, D_{eff}, using Equation 2.12. D_{eff} can then be used as a rough gauge of model accuracy. It cannot be a conclusive accuracy metric because of the ambiguity in the correction factor and because the real-world primary beams are not perfect (meaning the physical diameter does not necessarily equate to the primary beam-derived diameter). Additionally, not all antennas have the same tapering, but the use of Equation 2.12 as an accuracy metric assumes a tapering which is identical between all of the antennas. If the assumption is made that $D \sim \lambda/\theta_{\text{HPBW}}$, then it can be easily shown that a broader HPBW will drive the model diameter down. Because many of the antennas in the EVN have tapering, we can expect their HPBWs to be broader than their diameters suggested, meaning that we should expect D_{eff} to be less than the real diameters in most cases.

Another accuracy metric is to apply the models to the data from which they were derived and to attempt to derive the models again. If the models are accurate, then the primary beam attenuation should be largely eliminated within the HPBWs of the antennas. A more quantitative way of estimating the accuracy in this way is to calculate the standard deviation of the corrected amplitudes (Herrera Ruiz et al., 2018). A low standard deviation means the amplitudes of the visibilities corresponding to positions away from the phase centre (where $l = m = 0$) are close to the amplitudes of the visibilities corresponding to the central position of the FoV, i.e. the models are accurate. A final test can be conducted by applying the models to other widefield observational data and to see if the FoVs of the pointings increase.

2.3 Application of the models

The models can be applied in a few ways. The two main methods that will be discussed here are the A-projection algorithm (Bhatnagar, S. et al., 2008; Bhatnagar,

Rau, and Golap, 2013; Jagannathan et al., 2017) and the use of gain calibration tables (Morgan et al., 2011; Middelberg et al., 2011; Radcliffe et al., 2018). A third method, using a wide-band wide-field spectral deconvolution framework called DDFacet is also available to be used (Tasse, C. et al., 2018). Both the A-projection algorithm and DDFacet framework deconvolve DDEs during the imaging process, while the gain calibration tables act as Jones matrices to remove primary beam attenuation by adjusting visibility amplitudes directly. A-projection and gain calibration tables both have their advantages and disadvantages. A-projection is more accurate but computationally expensive. Gain calibration tables are not as accurate, but are much faster and cheaper computationally to apply. Gain calibration tables also only have to be applied once to the data, where A-projection has to be used during the generation of each image during the calibration process.

Consider the RIME, where it is assumed that all DIEs have been accounted for (i.e. $\boldsymbol{G}_p = \boldsymbol{I}$ for all p) and the only DDE present is primary beam attenuation of the array elements:

$$\boldsymbol{V}_{pq} = \iint_{lm} \frac{1}{n} \mathrm{E}_{pq}(l,m)\boldsymbol{B}(l,m)e^{-2\pi i\left(u_{pq}l+v_{pq}m\right)}\mathrm{d}l\mathrm{d}m. \tag{2.14}$$

In Equation 2.14, $\mathrm{E}_{pq}(l,m)$ cannot be removed from the integral as it is a function of l and m. This means that for the effects of each E_{pq} to be removed, it must be done in the image plane (Jagannathan et al., 2017). The inverse of the calibration model matrix, which is given by

$$\mathrm{A}^{M}_{pq,\nu,t} = E^{M}_{p} \circledast E^{M*}_{q}, \tag{2.15}$$

where $\circledast$ is the outer convolution operator, E^{M}_{p} and E^{M*}_{q} are models of the DDE beam matrices, ν is the frequency, and t the time value, is applied to the visibilities in a two-step process (Bhatnagar, Rau, and Golap, 2013). Note that the outer convolution operator is the same as the outer product operator, but it replaces multiplication with convolution. Nonetheless, in the first step, $adj(\mathrm{A}^{M*}_{pq,\nu,t})$ is convolved with the beam-convolved visibilities during the convolutional gridding steps in the imaging algorithms. The second step is dividing the resulting image throughout with the determinant of the Fourier transform of the sum of A^{M}_{k}, where $k = (pq,\nu,t)$. These two steps together apply the inverse of the calibration model matrix to the data during imaging. For completeness, see Bhatnagar, Rau, and Golap (2013), who describes the A-projection algorithm in detail.

On the contrary, during a typical observation, specific locations in the sky are targeted. These locations are called fields. All visibilities relating to a specific field will have the same offset in the lm plane from the phase centre. Multiple phase centres can also be used, each with a known coordinate, to improve the accuracy of the applied models. These offsets will remain constant throughout the observation,

as the positions of typical celestial objects targeted by radio astronomical observations generally do not move appreciably during an observation (other than of course the Earth's rotation). This means that for visibilities associated with a specific field and phase centre, their E_p matrices become constant with respect to l and m. Due to this, the $\mathrm{E}_{pq}(l,m)$ term in Equation 2.14 can be removed from the integral and divided away by its inverse, which we model using E_{pq}^{M*}. Astronomy software packages such as AIPS and CASA allow for data selection based on field identifiers. This means that the attenuation for each antenna and each specific field can be calculated and used to generate gain calibration tables. The advantage of this method is that it can be done easily on the fly and can be applied permanently to the data, unlike A-projection. A disadvantage of this method is that it is imprecise when compared to projection algorithms such as A-projection. It can however be used to create mosaicked images (Radcliffe et al., 2018).

In this thesis, we will be using the gain calibration table method to apply our derived primary beam models to the data. The design of the observation makes this method the most practical, which is made clear in Chapter 3.

Chapter 3

Observations and Data Calibration

3.1 ER052A

3.1.1 Observation

Primary beam models are typically obtained through OOF holography, which is a type of observation in which a bright point-source object is positioned in a grid of locations in the sky at various positions in the FoVs of selected antennae while being tracked by one or more antennae in the centre of their respective FoVs. In some cases, these models are also computationally derived using simulations of the antennae themselves (although these are less accurate). This type of observation is generally done with homogeneous arrays, but a slightly altered version can be used for heterogeneous arrays, which will be described below.

This observation was conducted on 28 February 2022 (EVN code: ER052A) using antennae from both the EVN and *e*-MERLIN (refer to Table 3.1 for the participating antennae). During this observation, J1048+7143 and 3C345 were the only sources observed, with 3C345 serving as the fringe finder and J1048+7143 acting as the target, bandpass calibrator, and additional fringe finder. The observation was centred on 1.6 GHz with eight spectral windows (spws) for the EVN sites and four spws for the *e*-MERLIN sites, with each spw comprising 32 channels at bandwidths of 0.5 MHz per channel. The measurements, for the most part, were made in two polarizations, left-circular (LL) and right-circular (RR), with a bitrate of 1024 Mbit s^{-1}. Measurements from UR and T6, which were in linear polarization, were converted to circular polarization using `PolConvert` (Martí-Vidal, I. et al., 2016). The *e*-MERLIN sites observed exclusively in LL polarization.

Following an initial 6.5-minute scan of 3C345, the observation proceeded with a routine wherein J1048+7143 was observed for approximately 2.3 minutes (except for the scan), followed by observations of four pointings, each lasting roughly the same duration. After four pointings were observed, J1048+7143's central position was again observed, and the routine was repeated. "Pointings" refer to the relative offsets of J1048+7143 within the FoVs of the antennae. They were arranged to form a $16' \times 16'$ grid centred on J1048+7143 and separated by steps of $2'$ in relative Right Ascension (RA) and Declination (Dec), which is depicted in Figure 3.1.

This is essentially a modified OOF holography observation in which each antenna acts as its amplitude reference and tracks its attenuation. For the primary beam of an antenna to be measured with a high enough density to be considered accurate, it should be sampled with a higher density than the critical sampling value, which is given by $\Delta\delta = \lambda/D_p$ (rad), where $\Delta\delta$ represents the maximum source position step size away from the centre of the FoV of the antenna in both the relative RA and Dec directions (Iheanetu et al., 2019). The oversampling factor in the case of ER052A is then given by $\Delta\delta(\text{arcmin})/2'$, which is recorded in Table 3.2 for each participating antenna.

The antenna beams can also be measured by tracking the relative changes in the autocorrelations of each antenna as the individual pointings are observed. Unfortunately, in the case of ER052A, the autocorrelations were normalised during the correlation process. Thus, this avenue of beam derivation is impossible in this paper but can be done in future work with new observations.

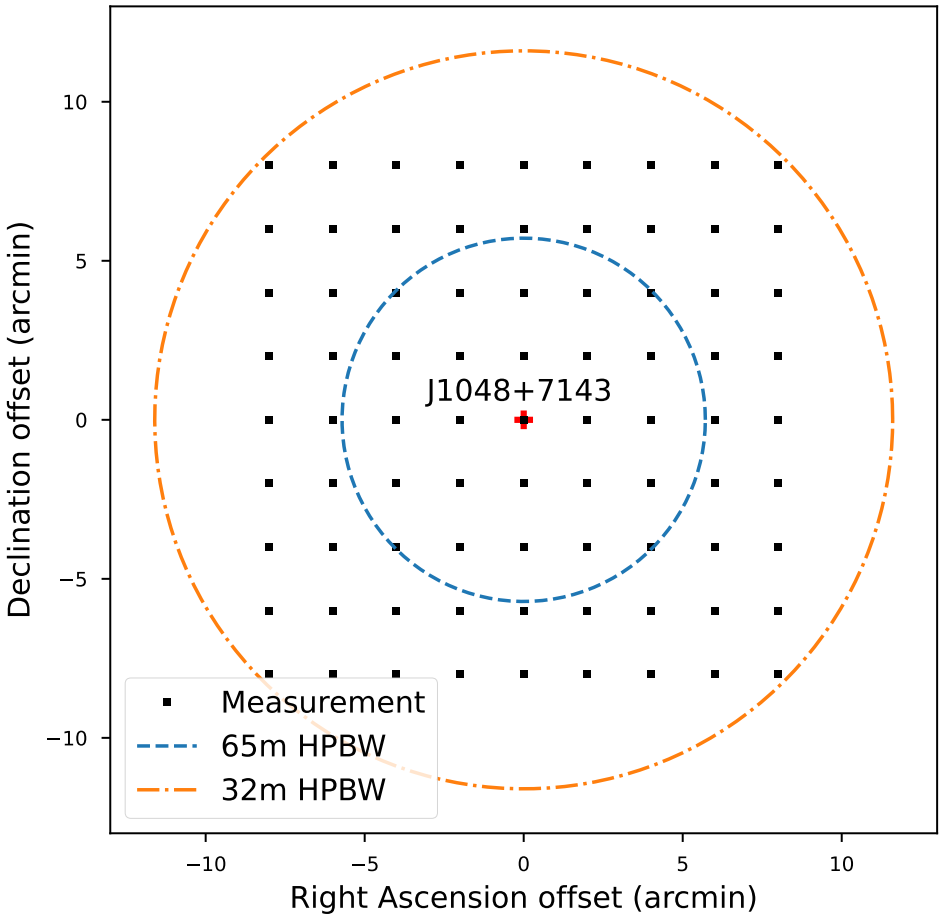

FIGURE 3.1: All the pointings and their offsets from J1048+7143.

TABLE 3.1: Antennae that took part in ER052A and N18L3 and some of their properties.

EVN code (CASA code)[a]	Name	Mount type	Diameter (m)
ER052A			
Wb (WB)	Westerbork	Equatorial	25
Ef (EF)	Effelsberg	Alt-Az	100
Mc (MC)	Medicina	Alt-Az	32
Nt (NT)	Noto	Alt-Az	32
On85 (O8)	Onsala	Equatorial	25
Tm65 (T6)	Tianma	Alt-Az	65
Ur (UR)	Urumqi	Alt-Az	25
Tr (TR)	Torun	Alt-Az	32
Ir (IR)	Irbene	Alt-Az	32
MkII (JB)[b]	Jodrell Bank Mk-2	Alt-Az	38×25
Da (DA)	Darnhall	Alt-Az	25
Pi (PI)	Pickmere	Alt-Az	25
Kn (KN)	Knockin	Alt-Az	25
De (DE)	Defford	Alt-Az	25
Cm (CM)	Cambridge	Alt-Az	32
N18L3[c]			
Hh (HH)	Hartebeesthoek	Equatorial	26
Sv (SV)	Svetloe	Alt-Az	32
Zc (ZC)	Zelenchukskaya	Alt-Az	32
Bd (BD)	Badary	Alt-Az	32
Sr (SR)	Sardinia	Alt-Az	64

[a] Station codes as used by the EVN combined with the code for each station within CASA. EVN codes sourced from the EVN status tables (accessed 06/2024; https://www.evlbi.org/sites/default/files/shared/EVNstatus.txt).
[b] Both the Lovell (Jb-1) and Mark-2 (MkII) telescopes were scheduled to take part in the observation, but only one of them had data shipped. The model generated for CASA-labelled JB in this paper is consistent with an antenna much smaller than Jb-1, hence the labelling of Jb-2 as JB in this table.
[c] Only antennae not in ER052A and with acceptable models.

TABLE 3.2: Oversampling factors calculated at $\lambda = 0.18$ m for antennae in ER052A.

Station	Diameter (m)	Oversampling factor
WB	25	12.38
EF	100	3.09
MC	32	9.67
NT	32	9.67
O8	25	12.38
T6	65	4.76
UR	25	12.38
TR	32	9.67
IR	32	9.67
JB	25	12.38
DA	25	12.38
PI	25	12.38
KN	25	12.38
DE	25	12.38
CM	32	9.67

3.1.2 Data calibration

The data were calibrated using a combination of the Astronomical Image Processing System (AIPS; Greisen, 2003) and Common Astronomy Software Applications (CASA; CASA Team, 2022) packages, both developed by the National Radio Astronomy Observatory (NRAO). While a CASA-only approach was preferred, an issue with the FITS-IDI formatted data causes the scans with different names but the same delay tracking centre to become fused, rendering calibration in CASA alone difficult. To resolve this, the data were first imported into AIPS and then exported, after which they could be successfully imported into CASA. Before exporting from AIPS, station-provided flags and smoothed antenna tables containing system temperature ($T_{\rm sys}$) and antenna gain curves were applied. Additionally, the AIPS task ACCOR was used to correct the scale of the cross-correlations amplitudes using measurements of auto-correlation spectra, and ionosphere-induced dispersive delays were corrected using total electron content measurements.

In CASA, some additional flagging was done. This included edge channels in the spws, the first few seconds of scans, radio frequency interference (RFI) removal and some erroneous scans from JB. Subsequently, instrumental and atmospheric delays were calculated, and bandpass calibration was performed using J1048+7143 and some pointings with small offsets, which were then applied to all pointings. Four rounds of phase-only self-calibration were conducted, followed by one round of amplitude-phase self-calibration on J1048+7143, with the latter employing normalized solutions to preserve the flux density scale. Additional amplitude-phase self-calibration rounds did not improve the signal-to-noise ratio (SNRs), meaning

further self-calibration was unnecessary. The self-calibration solutions derived for J1048+7143 were also applied to the pointings, with no further self-calibration performed on these target positions. Pointing self-calibration was deemed unnecessary because the only difference between the offset pointings and J1048+7143 should be the amplitude attenuation introduced by the primary beams of the array elements, as they were still observing J1048+7143, but at an offset location in their primary beams.

3.2 N18L3

3.2.1 Observation

The EVN observation with N18L3 was a predecessor to ER052A and was also centred on a wavelength of 18 cm. It followed the same observational pattern as ER052A but used J2139+1423 as its beam-measurement source. It also had a larger step between pointings than ER052A (5 arcminutes instead of 2 arcminutes). N18L3 had some problems, such as undersampling of large antennae, no autocorrelations, and unreliable (and subsequently ignored) *e*-MERLIN measurements due to multiple issues. This observation is used as a supplement to ER052A since the latter observation did not include the Russian telescopes and had problems obtaining a model for the Torun antenna. Combining N18L3 with ER052A will allow for a wider range of models to be tested on EG078B since many of the antennae that ER052A did not include are included in N18L3. The antennae in this observation that were not included in ER052A and have acceptable beam models are listed in Table 3.1.

3.2.2 Data calibration

The calibration process was started by applying smoothed system temperatures in the antenna tables provided by the stations and the station-provided flags in AIPS. Parallactic angle corrections were then applied, followed by the correction of ionosphere-induced dispersive delays using total electron content measurements. In CASA, the AIPS data were converted to a measurement set and then edge channels were flagged along with the beginning of each scan. RFI was accounted for by filtering outliers and setting a maximum allowable brightness. Some individual channels were also found to have strong spikes and were subsequently flagged. The wide spws of N18L3 (64 channels each) allowed this flagging without losing large percentages of data.

After the flagging steps, instrumental delays were corrected using two minutes of data from the first scan of J2139+1423. According to the observation logs, Jb-1 only joined the observation from the fourth scan onwards, but this station is flagged entirely in all scans in the data obtained from the EVN archive. All other antennae

were observed during the first scan, which allows it to be used to determine the instrumental delays. Next, the atmospheric delays were calibrated using a solution interval of 40 seconds, which divided each scan into two equal sections. Bandpass calibration was then conducted using J2139+1423. The solutions were not normalised to increase the brightness levels measured by some antennae that were lower than the more sensitive antennae, such as Effelsberg.

A single iteration of delay self-calibration was then done to supplement the a priori delay calibration. Afterwards, four iterations of phase-only self-calibration were completed. The solution intervals were set such that each scan of J2139+1423 was divided into equal sections. The corrections derived by these steps were small, showing no substantial phase errors left in the data and that a priori calibration solved many of the delay-related problems. After these steps, three amplitude-phase self-calibration steps were run with solution intervals three times larger than their counterpart phase-only self-calibration steps. The solutions were also normalised to preserve the flux density scales of the data.

3.3 EG078B

The EVN observation, EG078B, was chosen as a test base for the models derived from ER052A. It was originally conducted as part of the research for the work done by Radcliffe et al. (2018). It is a wide-field VLBI survey of the Northern region of the Great Observatories Origins Deep Survey-North (GOODS-N). This observation included EF, WB, O8, NT, TR, SV, BD, ZC, Jb1 (Lovell Telescope), and SH (Sheshan in China). Only four of these antennae have models derived from ER052A. Three of the missing models can be obtained from the results of N18L3. The data of EG078B were calibrated using the same steps taken by Radcliffe et al. (2018), excluding the multi-source self-calibration (MSSC; Radcliffe et al., 2016) and primary beam correction.

Ignoring the calibrator scans, only five fields were observed in EG078B. The main field is a pointing centred on the Hubble Deep Field North (HDF-N). The scans of this field included all of the antennae that participated in the observation. The four other fields are offset pointings containing only the large antennae, EF and JB (the Lovell telescope). This was done to keep a uniform sensitivity profile over the first central field (after applying estimated primary beam models). The fields are depicted in Figure 3.2.

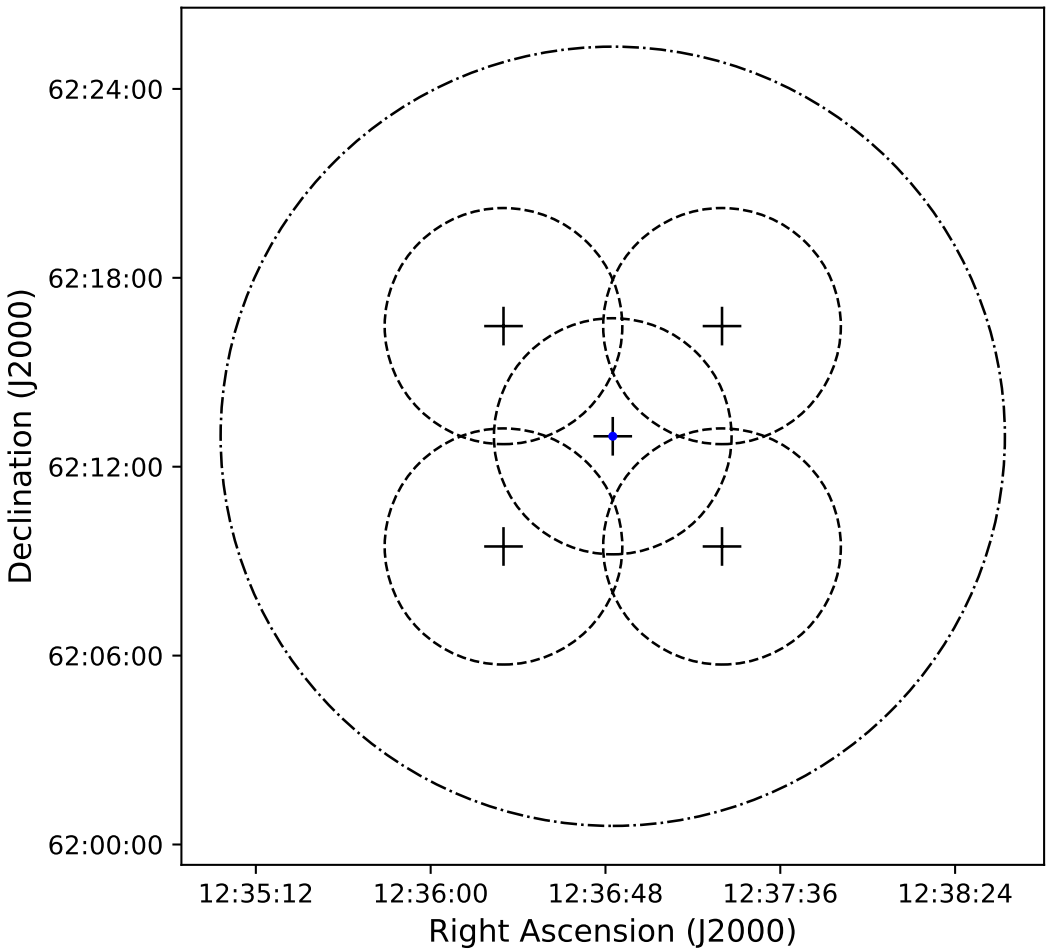

FIGURE 3.2: The pointings of EG078B. The EF-JB pointings only included Effelsberg and the Lovell telescope. The outer circle indicates the HPBW of Westerbork. The inner circles depict the HPBW of Effelsberg.

Chapter 4

Results

4.1 Model derivation

4.2 ER052A

Figure 4.1 shows the plots of the derived primary beams of all antennae in ER052A, with all derived parameters in Table 4.1. Figures 4.2 and 4.3 are identical to Figure 4.1, but are coloured by parallactic angle and elevation, respectively. The corrections were derived by setting the model of each pointing to be a normalised point source and then deriving amplitude corrections according to the deviation of each pointing from the model. The CASA task `gaincal` was used for this purpose. The corrections for RR and LL were combined to form a single dataset for each antenna due to the assumption that beam squint was not a factor. The corrections were then extracted from the output gain calibration table and used to fit a Gaussian model as given by Equation 2.10 to each antenna by a Python script making use of NumPy (Oliphant, 2006; Van Der Walt, Colbert, and Varoquaux, 2011) and SciPy (Virtanen et al., 2020). The SciPy function `curve_fit`, which employs the Levenberg-Marquardt algorithm for least-square fitting for unconstrained problems, was utilised to fit the models. Outlier filtering based on the interquartile range was also done on the corrections.

The uncertainties in the corrections were taken as the `PARAMERR` column in the `gaincal`-generated table. The difference between the average required correction at each offset and unity was multiplied with 0.25 and added to each `PARAMERR` value corresponding to the offset. This was done to account for the increasing expected asymmetries in the data due to the attenuation. The final errors were then supplied to `curve_fit`. The `curve_fit` function also gave the uncertainties in a and b (Δa and Δb) as output. Subsequently, D_{eff} was calculated for each model using Equation 2.12 for $\lambda = 18$ cm. The error in D_{eff} was determined according to

$$\Delta D_{\text{eff}} = \left| \frac{\mathrm{d}D_{\text{eff}}(b)}{\mathrm{d}b} \right| \Delta b = \frac{\lambda}{2\sqrt{2\ln(2)}b^2} \Delta b, \tag{4.1}$$

where b and Δb have been converted to radians.

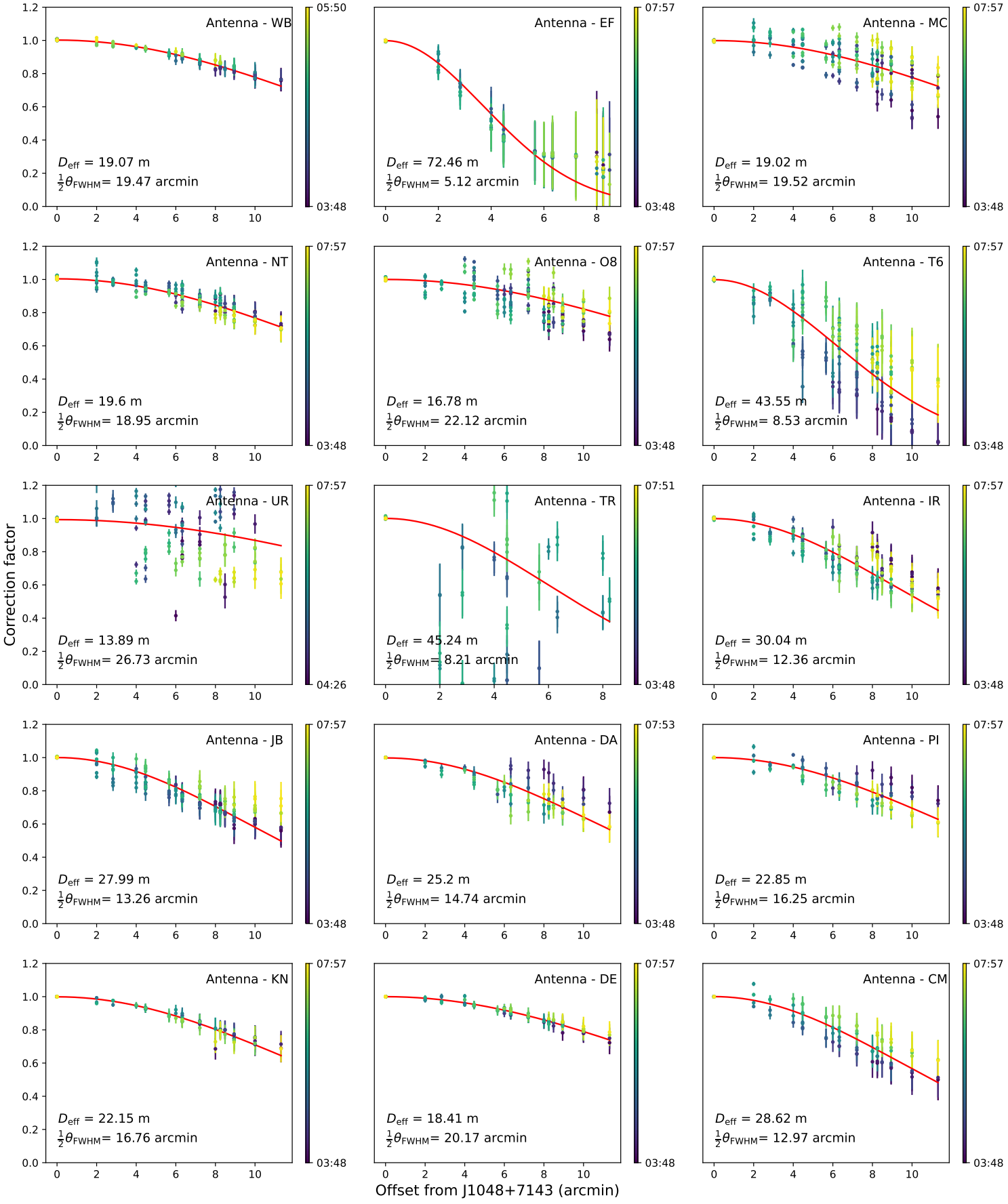

FIGURE 4.1: Derived models for the primary beams of antennae in the EVN and *e*-MERLIN participating in ER052A coloured by time. The red line in each plot is the Gaussian model fitted to the antenna data in question.

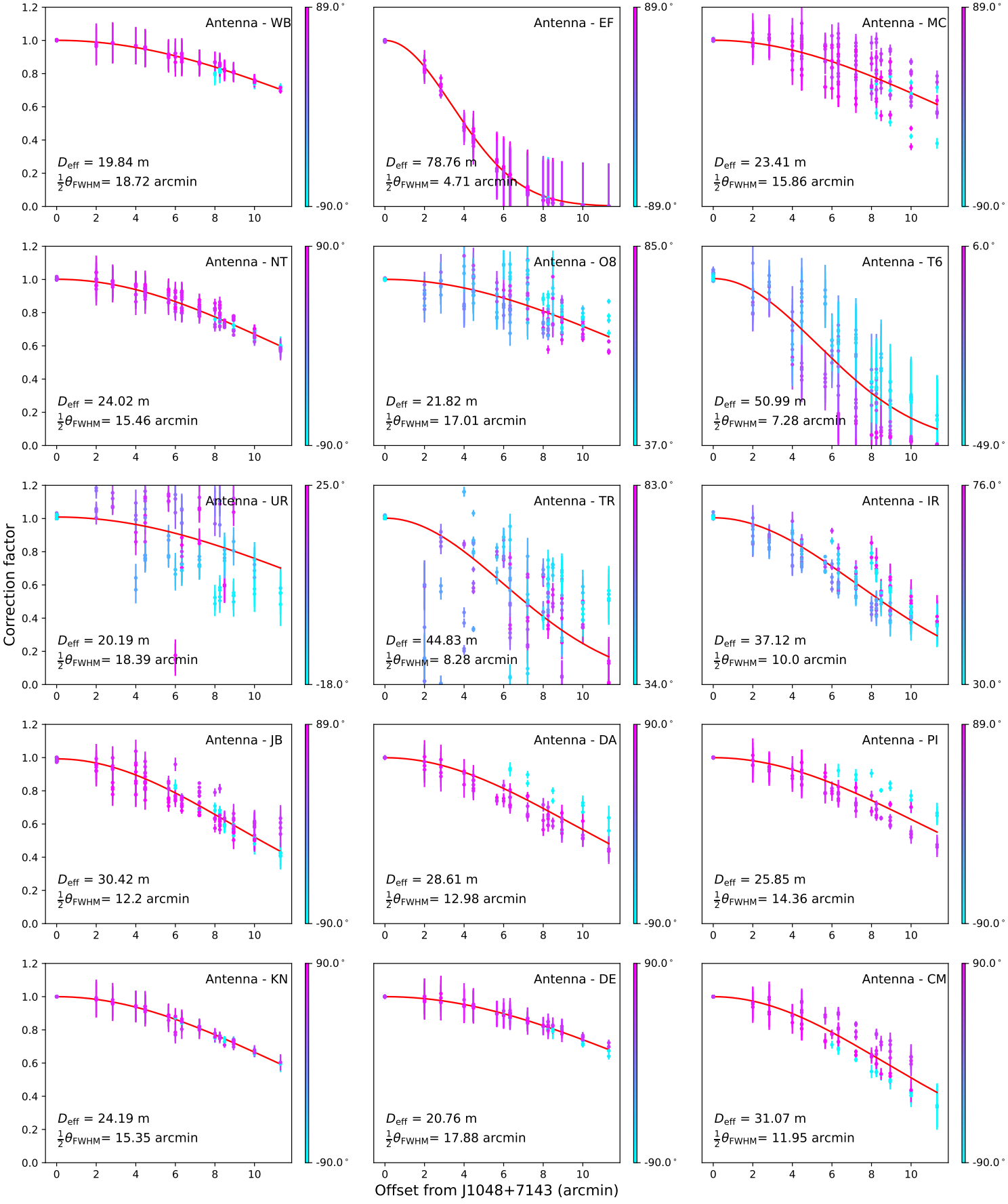

FIGURE 4.2: Derived models for the primary beams of antennae in the EVN and *e*-MERLIN participating in ER052A coloured by parallactic angle. The red line in each plot is the Gaussian model fitted to the antenna data in question.

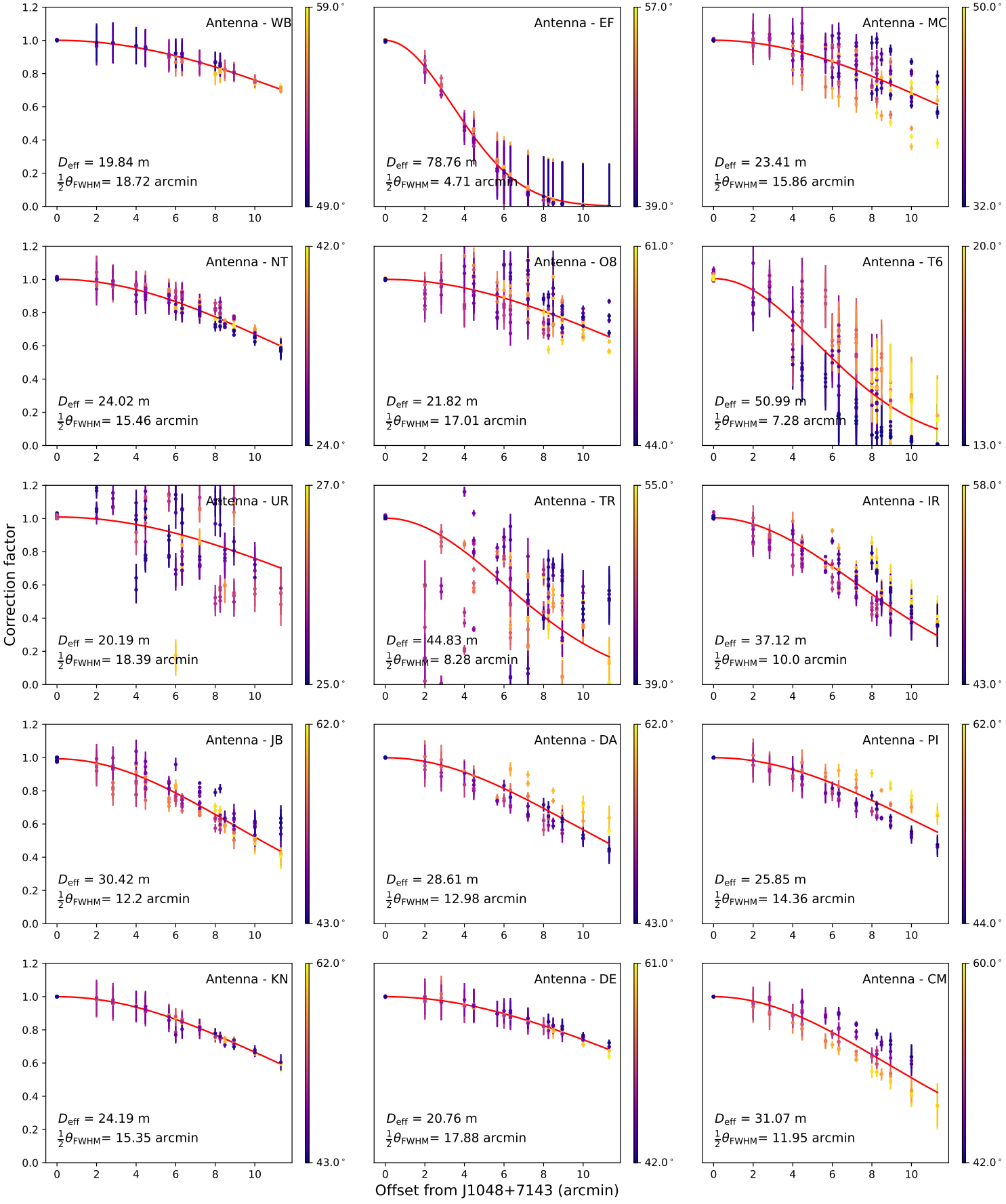

FIGURE 4.3: Derived models for the primary beams of antennae in the EVN and *e*-MERLIN participating in ER052A coloured by elevation. The red line in each plot is the Gaussian model fitted to the antenna data in question.

TABLE 4.1: Derived model parameters for the participating antennae in ER052A. The uncertainties in a and b were calculated by the `curve_fit` SciPy function and the errors in D_{eff} were calculated using standard error propagation rules applied to Equation 2.12 for $\lambda = 18$ cm.

Station	a (Jy/beam)	b (arcmin)	D_{eff} (m)
WB	1.001 ± 0.0003	13.512 ± 0.053	19.84 ± 0.08
EF	1.000 ± 0.0003	3.403 ± 0.018	78.76 ± 0.42
MC	1.001 ± 0.0028	11.449 ± 0.253	23.41 ± 0.52
NT	1.001 ± 0.0009	11.16 ± 0.071	24.02 ± 0.15
O8	1.001 ± 0.0019	12.282 ± 0.181	21.82 ± 0.32
T6	1.005 ± 0.0015	5.257 ± 0.154	50.99 ± 1.49
UR	1.009 ± 0.0028	13.278 ± 1.048	20.19 ± 1.59
TR	1.002 ± 0.0047	5.978 ± 0.232	44.83 ± 1.74
IR	1.005 ± 0.0018	7.221 ± 0.083	37.12 ± 0.43
JB	0.992 ± 0.0018	8.810 ± 0.092	30.42 ± 0.32
DA	0.999 ± 0.0031	9.368 ± 0.176	28.61 ± 0.54
PI	1.000 ± 0.0035	10.369 ± 0.188	25.85 ± 0.47
KN	1.000 ± 0.0007	11.081 ± 0.047	24.19 ± 0.1
DE	1.000 ± 0.0008	12.91 ± 0.070	20.76 ± 0.11
CM	1.000 ± 0.0029	8.626 ± 0.154	31.07 ± 0.55

4.3 N18L3

The beam models derived from N18L3 are given in Table 4.2 and depicted in Figure 4.4. The process of obtaining the models is identical to that of ER052A. The uncertainties were also determined in the same way. The parallactic angle and elevation colourisation schemes were not implemented for this observation, but it must be noted that both of these factors likely affect the quality of these models as with ER052A.

4.4 Models applied to ER052A

The CASA task `gencal` was used to generate calibration tables for each pointing, which were then applied to the post-self-calibration data using the `applycal` task in CASA. Afterwards, the same step was run as in Section 4.1, whereby the primary beam corrections were derived again. If the applied models are accurate and the data do not contain errors, the resulting corrections should be constant at the same brightness level as J1048+7143 within the HPBWs of the antennae. Figure 4.5 shows the result of this model application. In all cases, a was set to 1 to normalise the primary beams. All models applied were derived using ER052A.

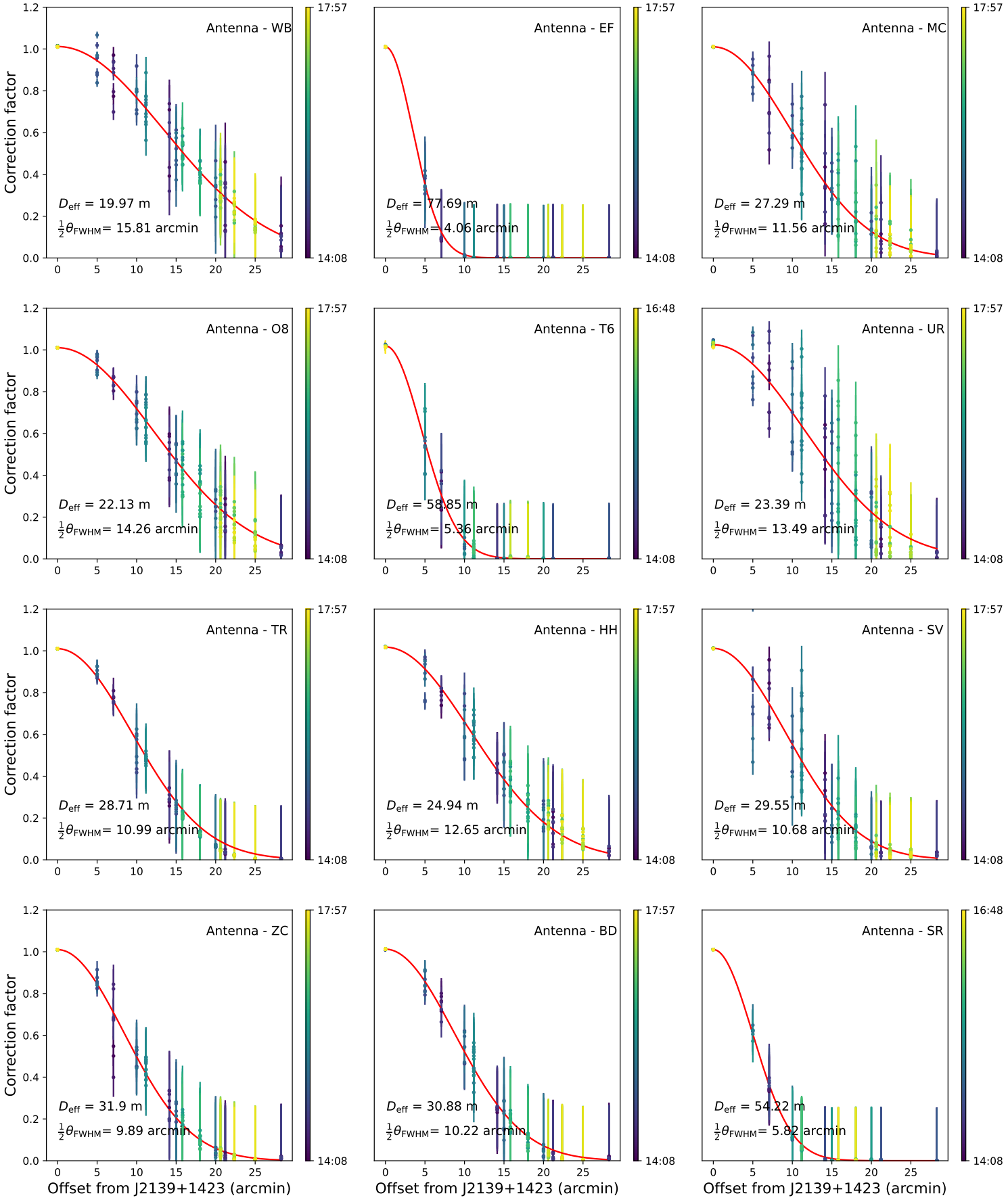

FIGURE 4.4: Derived models for the primary beams of antennae in the EVN and *e*-MERLIN participating in N18L3 coloured by time. The red line in each plot is the Gaussian model fitted to the antenna data in question.

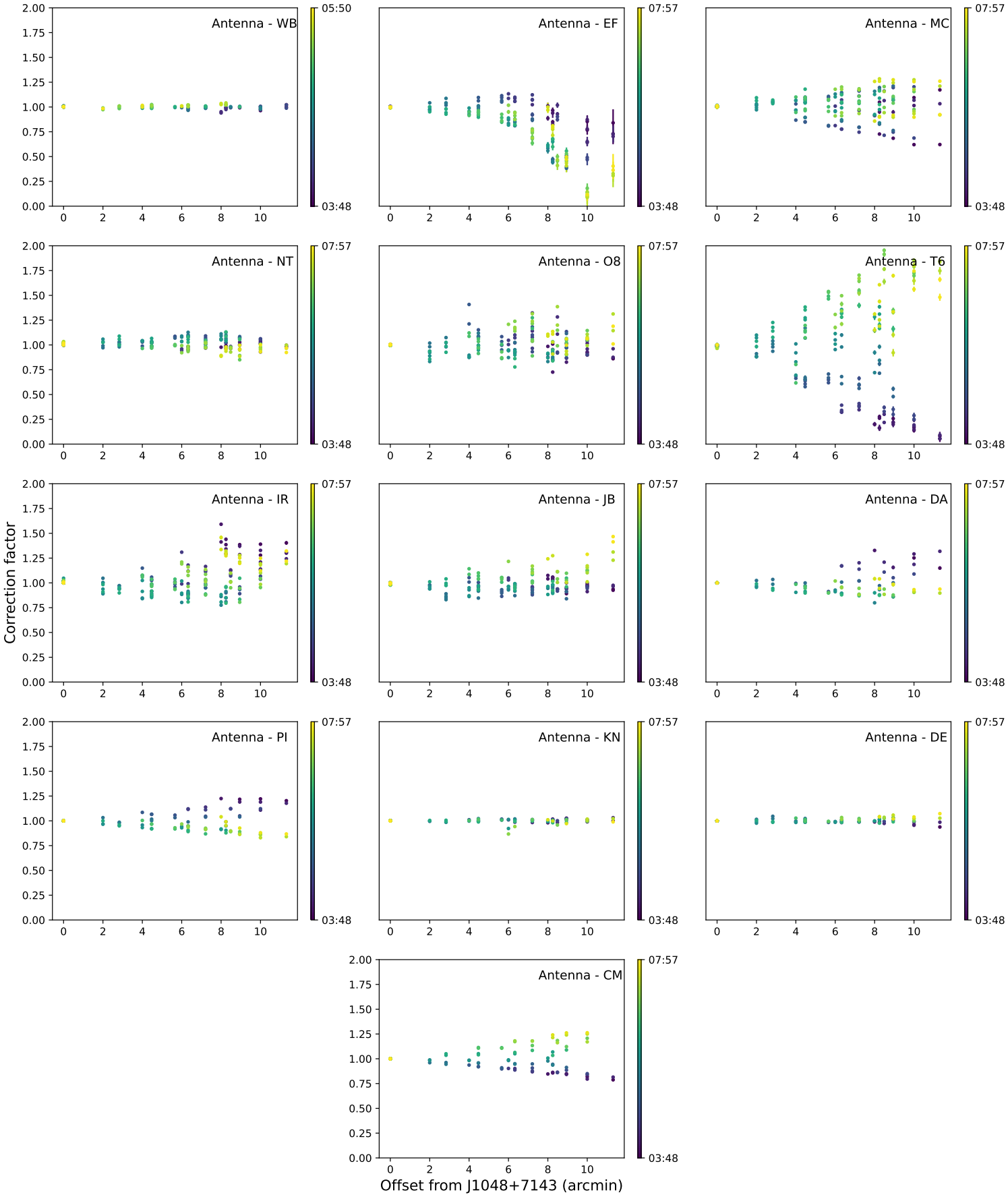

FIGURE 4.5: Corrections derived after application of derived antenna models. The colouring map is identical to Figure 4.1. The y-axis of each plot was scaled to a minimum of 0 and a maximum of 2.

TABLE 4.2: Derived model parameters for the participating antennae in N18L3. The uncertainties in a and b were calculated by the `curve_fit` SciPy function and the errors in D_{eff} were calculated using standard error propagation rules applied to Equation 2.12 for $\lambda = 18$ cm.

Station	a (Jy beam^{-1})	b (arcmin)	D_{eff} (m)
WB	1.012 ± 0.0007	13.424 ± 0.263	19.97 ± 0.39
EF	1.010 ± 0.0001	3.450 ± 0.016	77.69 ± 0.36
MC	1.010 ± 0.0006	9.821 ± 0.166	27.29 ± 0.46
O8	1.010 ± 0.0005	12.113 ± 0.129	22.13 ± 0.24
T6	1.019 ± 0.0008	4.555 ± 0.065	58.85 ± 0.84
UR	1.025 ± 0.0023	11.459 ± 0.325	23.39 ± 0.66
TR	1.010 ± 0.0002	9.334 ± 0.059	28.71 ± 0.18
HH	1.018 ± 0.0008	10.747 ± 0.130	24.94 ± 0.30
SV	1.012 ± 0.0009	9.071 ± 0.222	29.55 ± 0.72
ZC	1.010 ± 0.0004	8.403 ± 0.086	31.90 ± 0.33
BD	1.012 ± 0.0004	8.681 ± 0.065	30.88 ± 0.23
SR	1.010 ± 0.0001	4.943 ± 0.019	54.22 ± 0.20

Chapter 5

Discussion

5.1 The derived models

Many antennas have relatively small spreads in the required corrections at each offset (see Figure 4.1). This indicates that, in most cases, major asymmetries do not exist in the beams and that the models are likely to be accurate. Some potential asymmetric and time-dependent beam problems with some antennas are discussed in the subsequent sections. Effelsberg, for instance, has small spreads in the beam corrections, which, combined with its high sensitivity, shows why it is favoured as a reference antenna during data calibration of EVN observations. Many of the pointings are in the sidelobes of Effelsberg, but their amplitudes dropped to zero during data calibration. The same should be the case for the sidelobes of Tianma (such as in N18L3), but this does not seem to occur.

Effelsberg's intricate sidelobe structure can be seen in Figures 4.1 through 4.3 starting at around 6 arcminutes. This station also has small spreads in the beam corrections, which, combined with its high sensitivity, shows why Effelsberg is favoured as a reference antenna during data calibration of EVN observations. The sidelobes for Tianma should also be visible in these figures, but the relatively large spreads present in its corrections make it difficult to detect where they begin.

Westerbork's model is interesting as the station is in a unique position compared to the rest of the antennas. Its primary beam is described by a known polynomial, $\cos^6(c\nu\theta)$, where $c = 68$ at GHz frequencies, $\theta = \sqrt{l^2 + m^2}$ (degrees), and ν is the frequency in GHz (Popping, A. and Braun, R., 2008). This can be compared to the model derived here to find similarities and differences in the models. According to Hogbom and Brouw (1974), the HPBW of the Westerbork antenna at 1.415 GHz is $36'$, which is roughly equal to $30.6'$ when scaled to the central frequency of ER052A at 1.67 GHz. The applied model here has an HPBW of roughly $38.9'$. The minimal spread present in the required beam corrections for Westerbork also indicates an incredibly symmetric beam, which aligns with Casse and Muller (1974)'s statement that the beam is nearly perfectly circular.

Considering the Italian telescopes, Noto has small spreads in its beam corrections in Figure 4.1, which again implies symmetric measurements and a weak time

dependence, which is good. This along with its results in Figure 4.5 indicates that the model is accurate. Its relatively low D_{eff} compared to its real diameter is initially a concern, but it is actually not necessarily indicative of a problem as is shown in Chapter 6. Medicina has a broader distribution of corrections than Noto, but its results post-model application are also a positive indication. It has nearly the same relationship between its model and real diameters.

The *e*-MERLIN telescopes also seemingly have rather good models, which have low spreads and generally complete elimination of attenuation post model application. The spreads in the corrections for Knockin and Defford are well below 10% generally, which is also reflected in their results after model application. Cambridge has a time dependence present in its data, which seems to be caused by the parallactic angle change of the source during the observation (see Section 5.3.1). Darnhall seems to be suffering from asymmetries and an inconsistent attenuation rate, which again seems to be a parallactic angle problem. All of the *e*-MERLIN stations use Alt-Az mounts, so it should be expected that all of them are affected by the parallactic angle problem to some degree. Pickmere has around a 20% spread in its corrections generally, which is high, but its attenuation rate seems consistent. Its results after model application are also indicative of a somewhat accurate model.

The Jodrell Bank result indicates that the Lovell telescope is not included in the data and that the Mk-II telescope has been mislabeled - since its derived diameter is $\sim$ 28 m, which is around 50 m smaller than the Lovell Telescope. The derived diameter fits the Mk-II telescope closer, as it has a diameter of around 38 m. This telescope, however, is not a purely parabolic antenna and is thus expected to have an entirely different response pattern than the models assume. It should therefore then be expected that some asymmetries will be present in the results. The errors calculated for the *e*-MERLIN sites shown in Table 4.1 are also relatively low and thus indicative of somewhat accurate models. As mentioned with the Italian telescopes, the derived model diameters are generally somewhat less than the real diameters, but this can be explained quite easily.

The models for Onsala and Irbene as shown in Figures 4.1 through 4.3 do have some questionable features. In both cases, there are some inconsistencies in their attenuation rates and correction spreads. A problem which seems to be present in nearly every antenna is a strong correction time dependence at the pointings with large offsets. The results for the aforementioned two antennas in Figure 4.5 are indicators of good models, especially in the case of Onsala. In the case of Irbene, there is a slight upward bend at the large-offset pointings. The uncertainties in the derived model for Onsala do also indicate some potential inaccuracies in the model since they are quite high compared to other antennas with results considered accurate (such as Westerbork).

Torun and Urumqi had errors that were too large to be accepted. Both of these antennas were thus ignored when applying the models, so they are not present in

Figure 4.5. Potential reasons for the problems encountered with these models are discussed further in the following sections and subsections.

5.2 Model derivation process

Data can be combined in various ways during calibration steps. An example of such a combination is combining data from all the spws to form a single spw. This is generally done during calibration steps to improve the SNRs of the data and during steps where the effect being calibrated does not depend significantly on the frequency range covered by the combined data. Various data combinations were tried when attempting to derive the models. This included selecting only the central few channels for each spw and deriving a separate model for each spw, selecting all channels in each spw and again deriving a model for every spw individually, and finally combining all spws into one and selecting all resulting channels. The latter option is represented by the results shown in Section 4.1. This was the chosen method because it increases the SNRs of the data, and the frequency range covered by all the spws does not lead to significant changes in the primary beam shape, as Figure 5.1 illustrates.

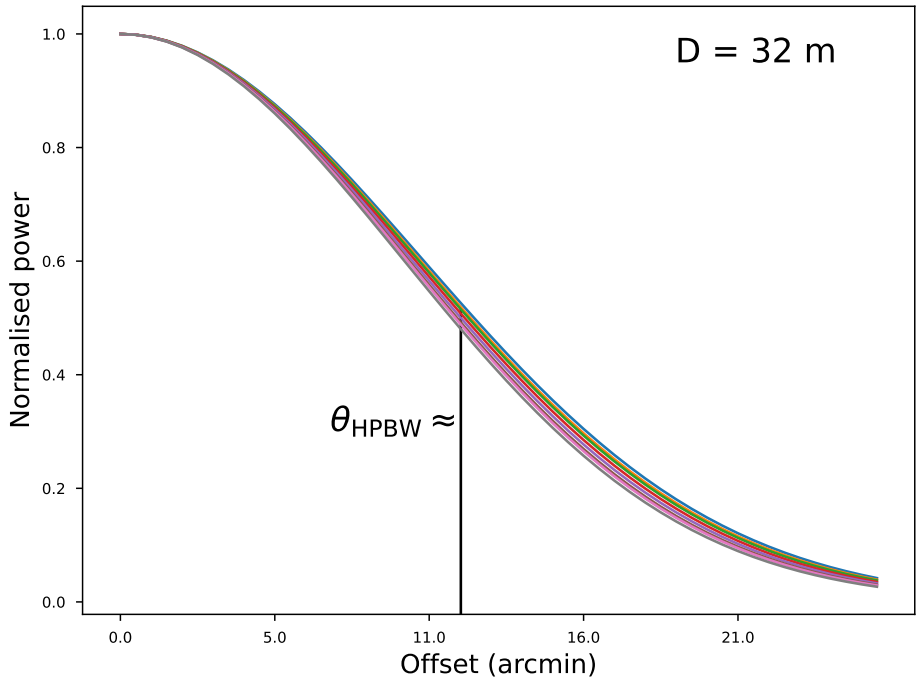

FIGURE 5.1: Gaussian primary beam models scaled to the central frequency of each spw in ER052A. Each model was derived using $K = 1.2$ and $D = 32$ m.

Some antennas had RFI-related problems, which complicated the spw and channel selection process. For instance, the central channels in the last spw (frequency range $\approx$ 1706–1722 MHz) were flagged in the case of Urumqi (in ER052A) due to RFI. Tianma had a similar problem in this spw, but automatic flagging procedures reduced the RFI.

The solution interval option in `gaincal` also underwent various iterations throughout derivation. We finally settled on a solution interval equal to the scan length, such that a correction is determined at the start and end of each scan. Doing this ensures that the only amplitude-related effect being calibrated is the primary beam of each antenna. The number of solutions present in Figures 4.1 through 4.3 for each antenna also serves as an indication of the percentage of its data that were flagged, with fewer solutions compared to other antennas, signifying less available data (due to flagging) or low SNRs (the minimum required SNR was set as 3). Torun is an example of this.

5.3 Origin of the errors

Some antennas have some noticeable spreads in their required corrections. This suggests the presence of asymmetries in their data, even within the HPBWs of several antennas. These asymmetries are due to amplitude and phase errors in the data after the calibration process. There are various potential causes for this. The first is that the calibration process was inadequate and has to be improved. Many different combinations of calibration steps were tried in this paper, which leads to the conclusion that the calibration process that was settled on is likely robust enough to account for significant problems. A second cause can be the time dependence of the primary beam shapes of the antennas. Many factors could lead to such a time dependence, some of which will be discussed in the following sections.

5.3.1 Asymmetric beams

All antennas undoubtedly have some form of blockage, which leads to asymmetric antenna responses. Figure 5.3 in this thesis showcases the differences between an aperture with strut and feed blockages and a perfectly illuminated unblocked aperture, the latter of which is assumed in the models. Further asymmetries could also occur because the antenna reflectors are not purely parabolic as assumed. In observations where measurements of various locations in the antenna beams are separated by time, these asymmetries would present as time-dependent variations in the amplitudes of pointings.

The change in the parallactic angle during the observation also complicates this further for the Alt-Az antennas as the sky rotates relative to their beams. Figure 4.2 shows the corrections coloured by parallactic angle as reference. It is made clear in

this figure that many of the ER052A antennas were affected by the parallactic angle change over time, especially for pointings with large offsets.

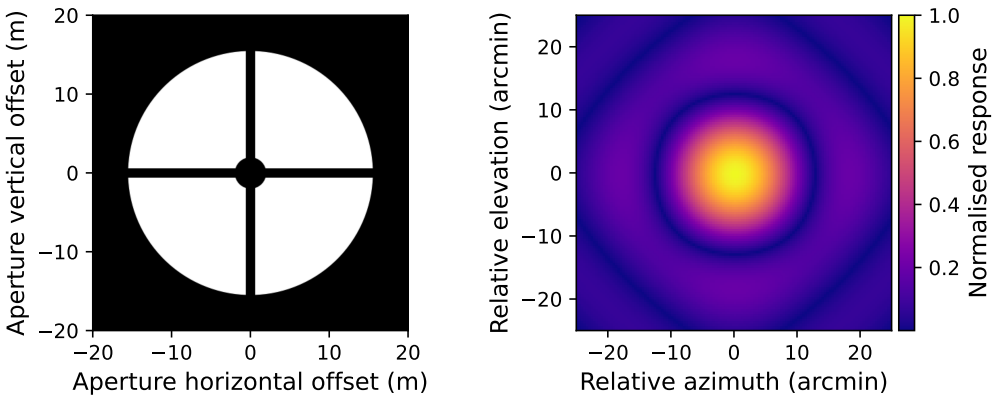

FIGURE 5.2: Aperture with strut- and feed-blockages (left) and its resulting voltage response pattern (right).

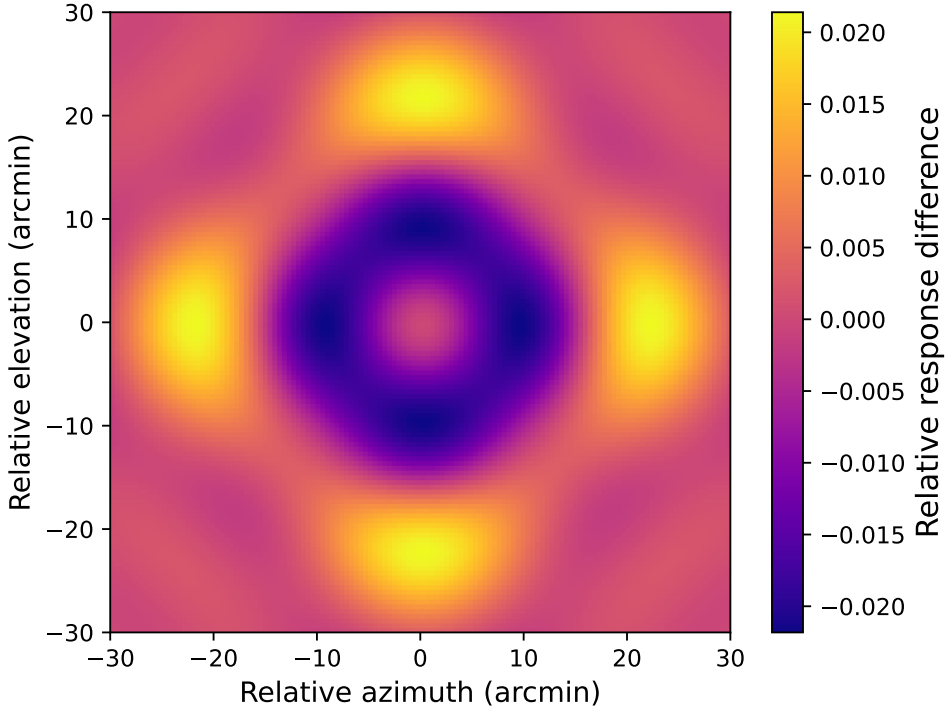

FIGURE 5.3: The differences between the power pattern of a circular aperture with struts and feed blockages and the pattern of an unblocked circular aperture. In each pixel, the response pattern of the latter was subtracted from that of the former.

5.3.2 Gravitational deformation

Many parabolic antennas are designed to undergo homologous deformation under the force of gravity, which means that their gravitationally deformed reflectors are still parabolic but with different focal lengths and potentially central axes (von Hoerner, 1967). This type of deformation can be modelled as a delay applied to the data due to the shift in the focal length (Artz, Springer, and Nothnagel, 2014). Some antennas considered in this paper have empirical models of their gravitational deformation-induced delays. They are Effelsberg (Artz, Springer, and Nothnagel, 2014), Medicina (Sarti, Abbondanza, and Vittuari, 2009), and Noto (Sarti, Negusini, and Claudio, 2011).

These models can be used in conjunction with Figure 4.3 to gauge the effect of gravitational deformation on the data from which the primary beam models were derived. In the case of Effelsberg, its elevation range in ER052A was 34° to 48°. This leads to a delay range of roughly −160 ps to −100 ps, where the negative sign indicates the signal path is shortened by gravitational deformation. In the case of Medicina, the elevation ranges from 29° to 44°. This leads to a delay range of 50 ps to 43 ps. Finally, Noto's elevation range is 22° to 38°, which leads to a delay range of roughly 23 ps to 17 ps (sourced from International VLBI Service for Geodesy and Astrometry (IVS) models[1]). These delays are somewhat less than the average delay calculated during multi-band delay calibration and substantially smaller than the average single-band delay correction. Suppose we assume that the models are at least somewhat representative of all the antennas in ER052A, especially antennas of similar sizes. In that case, we can conclude that gravitational deformation has some effect on the data but nothing substantial. These errors would likely also be calibrated during phase-only self-calibration.

5.3.3 T_{sys} tables

T_{sys} tables not accurately following the real-world temperatures could also lead to inconsistencies in the amplitudes of pointings at the same offsets. This could occur due to some gain instabilities in the antennas and inaccuracies in the temperature measurements. Outlier filtering of the station-provided T_{sys} curves had to be conducted using the `SNEDT` and `TYSMO` AIPS tasks during *a priori* calibration of ER052A, which greatly improved the resulting derived models. Tianma, Urumqi, Jodrell Bank, and all the *e*-MERLIN stations had constant temperatures and thus did not have to be filtered.

Torun can be seen in Figures 4.1 through 4.3 to have a large percentage of flagged data and quite unstable required corrections (it has an effective diameter of 51 m compared to a real diameter of 32 m). This is connected to the station-provided T_{sys} tables, as author-generated T_{sys} tables, which all had constant temperatures, led to

[1] https://ivscc.gsfc.nasa.gov/IVS_AC/apriori/gravity_deform_model_v2023-01-24.txt

a far lower flagged percentage and a greatly reduced spread in the beam corrections for this station. Using the author-generated tables led to larger spreads in the *e*-MERLIN stations and larger derived diameters generally. The aforementioned figures also display the sidelobes of Effelsberg, whereas the author-generated tables led to the sidelobes not being present in the data. Because of all these factors, it was concluded that the station-provided temperature tables led to more accurate models and that deriving a model of Torun was a lost cause. The same can generally be said for Urumqi, which seems to have a considerable time and parallactic angle dependence in the spread of its required beam corrections. The derived models of Torun and Urumqi were thus ignored, so Figure 4.5 is missing these two antennas.

5.4 Error analysis

An immediately noticeable difference between the models of N18L3 and ER052A is the larger correction uncertainties in Figure 4.4 compared to Figure 4.1. The general spread in the corrections is also wider in this observation than in ER052A, especially at large-offset pointings. This indicates that ER052A is a better observation to derive these models from. However, when comparing the uncertainties in Table 4.2 with those of Table 4.1, it can be seen that in the cases of Urumqi, Torun, and Medicina, the uncertainties associated with the N18L3 models are lower. This should be expected for the former two antennas, as the authors consider their ER052A models as too inaccurate and unreliable to be used for application. In the case of Medicina, the reason is not so apparent, as there are considerable spreads (comparable to its ER052A plot) present in its data.

Consider Onsala's models, where it can be seen that the uncertainties associated with the model derived from N18L3 are slightly smaller than the ER052A model and their parameters are within each other's uncertainty ranges. This indicates an agreement between the models. The models of Medicina do not have this relationship. Their uncertainties are slightly agreed upon, but the derived parameters differ substantially. Considering their plots in Figures 4.1 and 4.4, there seems to be a visible difference in their attenuation rates. Its attenuation in Figure 4.4 looks more natural, as in Figure 4.1 its smaller-offset corrections seem to have an inconsistent attenuation rate visible in its unnatural correction variation. The spreads in the corrections present in the N18L3 Medicina model are substantially larger on average than ER052A's model. This means that the latter model should be more accurate. The large antennas also have lower uncertainties in this observation than ER052A, but their undersampling makes them potentially inaccurate. Effelsberg in Figure 4.4 has no measurements within its HPBW, for instance, and Tianma has one offset within its HPBW.

Luckily, several antennas have rather decent models in N18L3. Among these are Torun, Hartebeesthoek, Zelenchukskaya, Badary, and Onsala. The model of Svetloe

can be arguably passed as "acceptable", but it has quite a considerable spread for the pointings with smaller offsets. The same can be said for the N18L3 model of Urumqi. It, too, has quite substantial spreads, but the errors associated with this model are quite lower than those in the ER052A model. These models will be included in the list of available primary beam models in the future. Still, they should be considered for further observations to obtain improved models with higher accuracies. N18L3 no doubt has some of the same problems regarding sources of asymmetries in the corrections since many of the antennas in this observation were in ER052A too. Interestingly, in most cases, there seems to be no real-time dependence in the corrections at each individual offset in Figure 4.4. Therefore, there must be other problems than ER052A faced since the model for Westerbork has much larger spreads in N18L3 than ER052A. The spreads in the corrections then indicate a likely elevation dependence in the corrections. In any case, it can be concluded that N18L3 is perfect for supplementing the models derived by ER052A.

5.5 Models applied to ER052A

The models successfully eliminate the overall effect of the primary beam attenuation when applied to ER052A for most of the antennas, as seen in Figure 4.5. Barring Tianma, the spreads in the post-application corrections are minimal. This indicates that the models likely have a large degree of accuracy. In the case of Effelsberg, applying the models beyond its HPBW can be seen as an upturn in the corrections that occur beyond ≈ 4.38 arcminutes. To combat effects like this, a restriction could be introduced based on the HPBW of the models, where the data of antennas where fields fall outside their HPBWs or primary beams could be flagged. This could stop primary beam-induced amplitude errors in the outskirts of wide-field observations.

Tianma again indicates a significant time dependence, where the earlier scans in the observation deviate dramatically from the later observations. The spread in Figure 4.5 for the Tianma post-model application is to be expected, considering the spread in the required corrections used to derive a primary beam model for this station. As mentioned before, this could be due to the parallactic angle change over time, as Figure 4.2 indicates quite a noticeable separation in the corrections for this station as the source parallactic angle changes, even within its HPBW.

The Westerbork antenna is also an interesting result, as the attenuation seems to be eliminated almost perfectly, combined with the small spread in the corrections both in Figures 4.1 and 4.5. This antenna uses an Equatorial mount, meaning it should be unaffected by parallactic angle (and according to Figure 4.2, it is). The antenna is also not large compared to other antennas in this observation, meaning the effect of gravitational deformation on this antenna is likely also minimal.

Chapter 6

Models Applied to EG078B

6.1 Results

The models were applied to the annulus fields (labelled HDFA) described in Radcliffe et al. (2018) using the VLBI pipeline by Radcliffe (2020), as well as the central fields (labelled HDFC). $3.47'' \times 3.47''$ images were then created of each field and scanned using a VLBI cataloger[1] making use of the Python Blob Detector and Source Finder (PyBDSF[2]). The CLEAN algorithm (Högbom, 1974) was employed for the imaging of these fields, but it was not done extensively. A series of different required detection thresholds were used in the cataloger, from 5σ to 9σ. Two sets of models were applied - one being estimated models (referred to as old models) and the second being the estimated models combined with the models derived in this paper (referred to as the new models).

Regarding the annulus fields, no detections were made with a detection threshold of 6σ and above. The new models detected 25 annulus fields with a detection threshold of 5σ and the old models detected 23. Many of these detections were slightly above 5σ, so the cataloger was run with an SNR threshold of 5.5σ. This reduced the detections to only four, all detected by both model generations. Regarding the central fields, the 5.5σ threshold was also used. The new models detected six sources, and the old models detected five. All of these detections are given in Table 6.1. Figure 6.1 compares the respective images of the HDFA detections, and figures 6.2 to 6.7 depict the same for the HDFC detections.

6.2 Discussion

6.2.1 The model generations

The purpose of applying the models to EG078B is to test them on real observational data and to compare their effects with those of an older set of models. The old models are based on the real diameters of the antennas and some previous research. Combining ER052A and N18L3 has allowed most of the antennas in EG078B to have

[1] https://github.com/jradcliffe5/General_VLBI_cataloger
[2] https://github.com/lofar-astron/PyBDSF

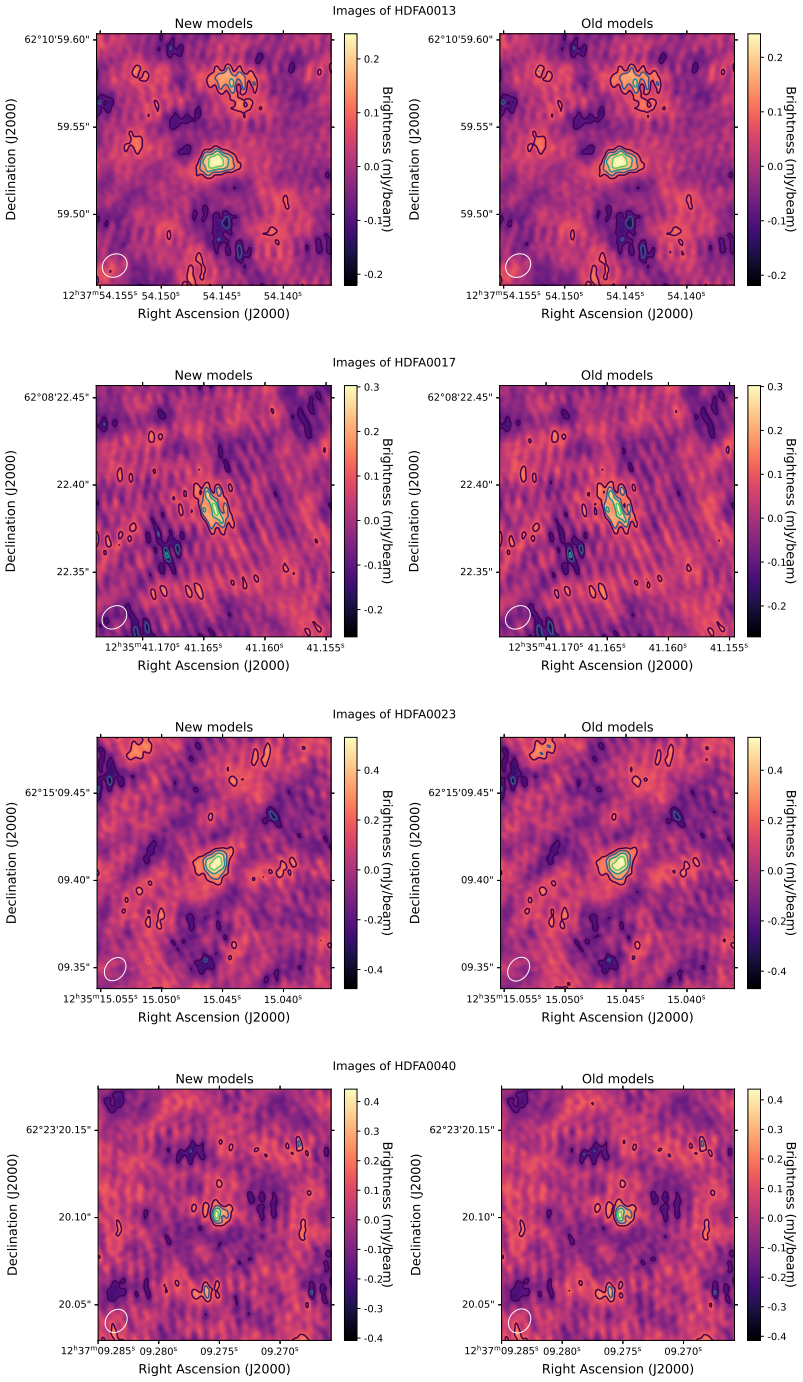

FIGURE 6.1: Images of HDFA fields with detections. The contours represent the SNR of the regions starting from 2 and ending at 6, with steps of 1. The brighter rings are the higher SNRs. The white ellipse represents the synthesised beam's size.

TABLE 6.1: Sources detected in the annulus fields of EG078B with a threshold of 5.5σ after application of primary beam models.

Field name	Right Ascension (J2000)	Declination (J2000)	SNR (New / Old)
HDFA0013	12:37:54.1457	+62:10:59.5315	5.89 / 5.90
HDFA0017	12:35:41.1642	+62:08:22.3850	5.66 / 5.58
HDFA0023	12:35:15.0457	+62:15:09.4100	5.57 / 5.63
HDFA0040	12:37:09.2754	+62:23:20.1016	5.55 / 5.51
HDFC0152	12:36:36.9970	+62:10:04.3690	5.50 / 5.37
HDFC0161	12:36:44.3858	+62:11:33.1720	9.33 / 9.28
HDFC0214	12:36:59.3326	+62:18:32.5670	53.35 / 51.65
HDFC0260	12:37:13.8690	+62:18:26.3040	8.95 / 9.76
HDFC0262	12:37:14.9389	+62:08:23.2230	53.41 / 51.92
HDFC0277	12:37:21.2517	+62:11:29.9630	6.91 / 7.15

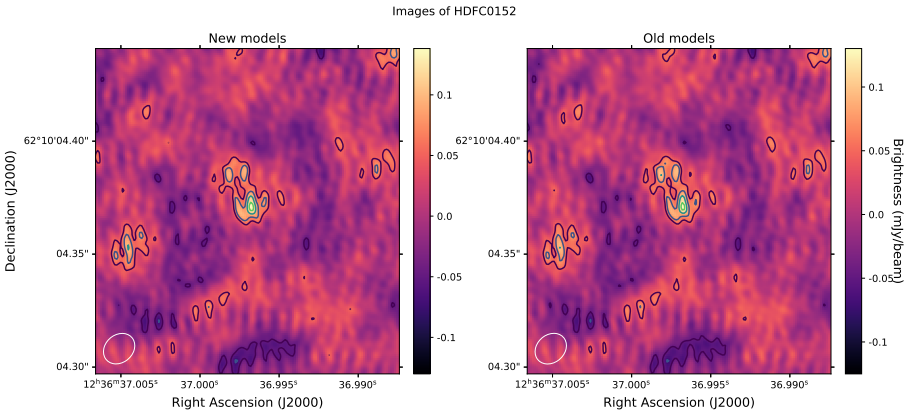

FIGURE 6.2: Images of HDFC0152. The contours represent the SNR of the regions starting from 2 and ending at 6, with steps of 1. The brighter rings are the higher SNRs. The white ellipse represents the synthesised beam's size.

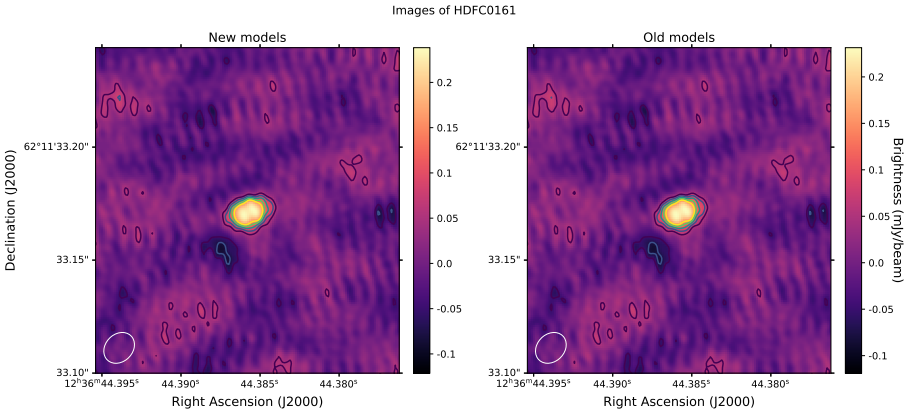

FIGURE 6.3: Images of HDFC0161. The contours represent the SNR of the regions starting from 2 and ending at 6, with steps of 1. The brighter rings are the higher SNRs. The white ellipse represents the synthesised beam's size.

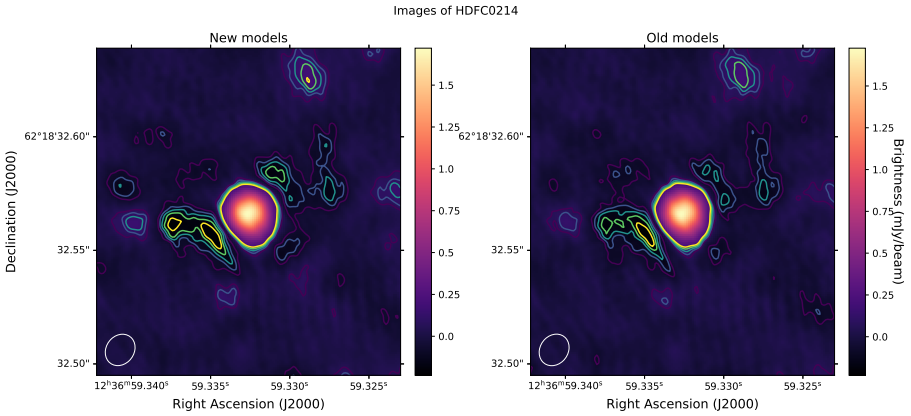

FIGURE 6.4: Images of HDFC0214. The contours represent the SNR of the regions starting from 2 and ending at 6, with steps of 1. The brighter rings are the higher SNRs. The white ellipse represents the synthesised beam's size.

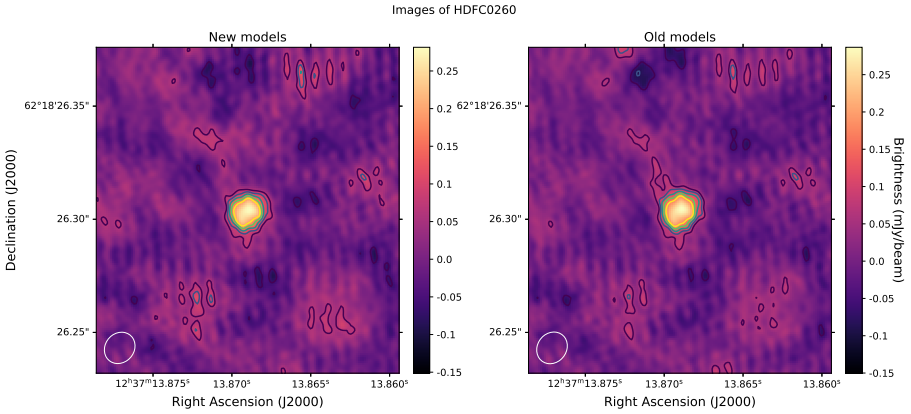

FIGURE 6.5: Images of HDFC0260. The contours represent the SNR of the regions starting from 2 and ending at 6, with steps of 1. The brighter rings are the higher SNRs. The white ellipse represents the synthesised beam's size.

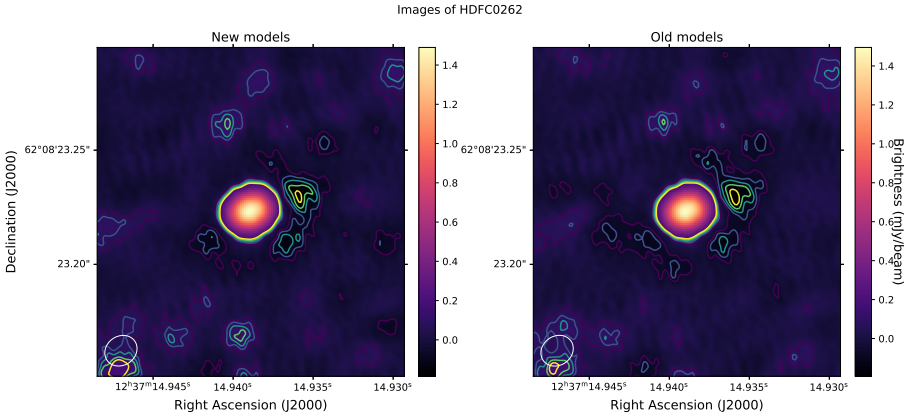

FIGURE 6.6: Images of HDFC0262. The contours represent the SNR of the regions starting from 2 and ending at 6, with steps of 1. The brighter rings are the higher SNRs. The white ellipse represents the synthesised beam's size.

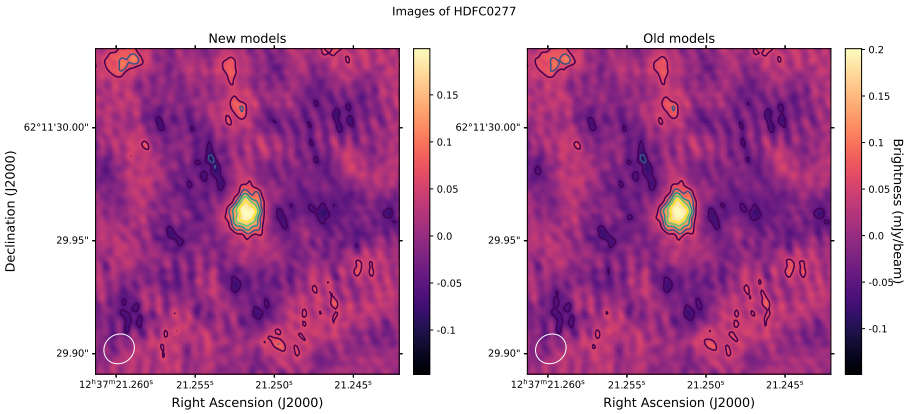

FIGURE 6.7: Images of HDFC0277. The contours represent the SNR of the regions starting from 2 and ending at 6, with steps of 1. The brighter rings are the higher SNRs. The white ellipse represents the synthesised beam's size.

TABLE 6.2: New models compared to old models for EG078B. In each case the HPBW was calculated as λ/D with $\lambda = 0.18$ m.

Antenna code	Old model D_{eff} (m)	New model D_{eff} (m)	ΔD_{eff} [a] (m)	ΔHPBW [b] (arcmin)
Ef	76	78.76	-2.76	0.28
Wb	25	19.84	5.16	-6.44
On85	25	21.82	3.18	-3.61
Nt	25	24.02	0.98	-1.01
Tr	25	28.71	-3.71	3.2
Sv	32	29.55	2.45	-1.6
Bd	32	30.88	1.12	-0.7
Zc	32	31.90	0.10	-0.06

[a] $\Delta D_{\text{eff}} = D_{\text{eff,old}} - D_{\text{eff,new}}$
[b] $\Delta\text{HPBW} = \Delta\text{HPBW}_{\text{old}} - \Delta\text{HPBW}_{\text{new}}$

new models. The Lovell and Sheshan telescopes still require new models, as they were absent from N18L3 too. They will thus still restrict the FoVs of future EVN observations, even with the other new models being made available.

Table 6.2 lists the differences in the models relevant to EG078B. The differences between the model diameters and resulting HPBWs (i.e. FoVs) were also determined in each case. In cases of a negative HPBW difference, the new models have larger FoVs and vice versa. Note that some antennas (notably Effelsberg) already had models based on earlier years' empirical research. It is unclear whether or not the old model of Noto was based on previous work as its diameter was given by 25 m, while the antenna has a real diameter of 32 m. The new model has a diameter of $\sim$ 24 m, which roughly agrees with the old model. The model diameter for Noto is $\sim$ 1.33 times smaller than its real diameter. This is similar to the relationship between the effective and the real diameter of the Effelsberg models and is thus within an acceptable margin.

Although initially somewhat alarming, the differences between the effective diameters of the model generations do not necessarily indicate a problem. The equation used to determine the D_{eff} values,

$$D = \lambda / \theta_{\text{HPBW}}, \tag{6.1}$$

does not take tapering into account. It can be done by introducing a factor on the right-hand side of the equation, typically 1.2 (Morgan et al., 2011; Condon and Ransom, 2016). The precise value of this "tapering factor" depends on the design of each antenna and will thus differ between the antennas in a heterogeneous array. The result of not introducing a tapering factor is that the broadened HPBW (i.e. larger θ_{HPBW} value) will reduce the derived D_{eff} value.

This means that it is generally expected for antennas initially designed for single-dish observations (most of the antennas in the EVN) to have smaller D_{eff} values since they all have tapering. The difference between their real-world and model diameters depends on the degree of tapering seen and, of course, the accuracy of the models - making it impossible to account for all types of tapering with a single factor. The best approach is, therefore, to not account for tapering at all through the formula but to allow the derived D_{eff} to be scaled accordingly during least-square fitting. This still relies on the attenuation to be measured accurately. Not enforcing a particular tapering factor also allows for any other factors that can affect the width of an antenna's primary beam to be incorporated into each separate model.

6.2.2 Detected sources

If the noise levels in the images follow a Gaussian distribution, then the number of synthesised beams above the SNR threshold (γ) present in the images can be determined according to,

$$\mathrm{N}_\gamma = N \left[1 - \text{erf}\left(\gamma/\sqrt{2}\right)\right] /2, \tag{6.2}$$

where N is the number of resolution elements in the image. N is given by

$$\mathrm{N} = \frac{A \times \overline{d}}{\Omega_b}, \tag{6.3}$$

where A is the image area, $\overline{d} = \pi\sqrt{12}$, $\Omega_b = \frac{\pi}{4\ln 2}\Theta_{\text{maj}}\Theta_{\text{min}}$, and Θ_{maj} and Θ_{min} are the major and minor axes of the synthesised beam of the relevant image (Middelberg et al., 2013). In our case, the synthesised beam size varies between the fields, but even with a high value of $\mathrm{N} = 1e6$, for SNR thresholds above 7, we have $\mathrm{N}_\gamma \sim 0$. With an SNR threshold of 5, this value goes up to around 0.3. This will vary from image to image since it depends on the synthesised beam's size. The maximum N_5 value found for the annulus fields is 0.21 and for the central fields, it is 0.18. Increasing the required SNR to 5.5σ yields a maximum value of 0.014, which is substantially

lower. Doing so also reduces the amount of detected sources in the annulus fields to 4 sources detected through both model generations.

Determining detected sources' validities is easier when combining data of different wavelengths. We used VizieR[3] to search various survey catalogues for co-detections of our sources in the X-ray, radio, and optical regimes. Our focus was on the annulus detections, and HDFC0152 since these are the only questionable sources requiring validation. The annulus fields also have implications for the performance of the model generations. We searched for detections within 1″ of our detection coordinates.

Only HDFA0013 had entries in the region around its central position in the X-ray Chandra Deep Field - North (CDF-N) survey (Xue et al., 2016). Regarding optical and near-infra-red detections, HDFA0013 (Barger et al., 2003; Hardcastle et al., 2023), HDFA0017 (Marton et al., 2024), HDFA0023 (Capak et al., 2004; Yang et al., 2014), and HDFC0152 (Hsu et al., 2019), all had detections in various surveys. Most of these detections are within a radius of $\sim$ 0.5″ from our source coordinates. In the radio wavelengths, HDFA0013 (Shimwell et al., 2022; Hardcastle et al., 2023), HDFA0017, HDFA0023, and HDFA0040 (Oliver et al., 2012) all had corresponding detections. These are positive indications that the detected annulus sources are indeed real. In the original study of the EG078B data, Radcliffe et al. (2018) did not include the detection made in this paper in HDFC0152 in their list of sources. This, along with the low SNR of this field indicates that as far as radio astronomy is concerned, this source is likely not a real source.

Tables 2 and 3 by Radcliffe et al. (2018) also indicate the significant decrease in source SNRs between the data used in this paper and the original study. HDFC0214, for instance, saw a decrease from 88.2 to 51.65. We believe that this happened because we did not use MSSC. The effect of not applying this calibration technique is further shown by the lack of detections in this paper compared to the 31 made by the authors mentioned previously. Regardless, now that we have demonstrated that the annulus sources detected likely are real, we can rest assured that the comparisons made between the model generations' performances in the following sections are valid.

6.2.3 Annulus fields

Almost no differences are visible in the HDFA detections between the images of the different model generations. This is mainly due to the low brightnesses of these sources, as we expect to see a larger difference between the models with brighter sources. We expect this because the errors induced by inaccurate primary beam models scale according to flux density because of their multiplicative nature. In fact, Natarajan et al. (2017) found that calibration errors have a greater negative effect

[3]https://vizier.cds.unistra.fr/

during the model fitting steps of the imaging of detected sources when dealing with SNRs much greater than 100. This gives another reason why accurate primary beam models are required. Thus, at the relatively low SNRs that these detections were made, we should not expect to find a large SNR difference between the model generations. In addition to this, these fields are also outside the HPBWs of the large antennas and thus lie in regions in which the array is far less sensitive.

The SNRs recorded in Table 6.1 should thus be taken with a grain of salt when used to compare the models using the annulus fields. The SNRs recorded in HDFA0013 were nearly identical, while HDFA0023 had a slightly higher recorded SNR through the old models. The new models recorded higher SNRs for the remaining annulus fields, with roughly the same margin as HDFA0023. With this severely limited sample size, the new models slightly outperformed the old models. Still, there are not enough samples to obtain a conclusive picture of model performance, especially with the low source brightnesses.

6.2.4 Central fields

HDFC0152 and HDFC0161 have relatively low SNRs compared to the rest of the central detected sources. In the case of HDFC0152, the old models' images did not reach the detection threshold, and the new models met the threshold exactly. Comparing this field's brightness levels to the other central fields reveals it is quite faint. As mentioned, this source has no X-ray or radio components (at least not listed on VizieR) and only an optical detection close to our coordinates. This, along with the small angular size of the source in Figure 6.2, indicates that this detection is likely a false detection. HDFC0161 is at least above the 6σ SNR threshold, and its central source is much more defined, which is expected of a real source. Yet, the images of the respective models for this source still look almost identical. The source is also listed in Tables 2 and 3 by Radcliffe et al. (2018), which indicates that it is a real source.

HDFC0214 is an incredibly bright source compared to the previous detections. More differences between the models are thus visible in its images (Figure 6.4). The areas with lower SNRs in the old-model images seem slightly lifted and expanded generally. The central source's SNR is also increased with $\sim$ 3.5%. There are no substantial emissions around the central source in both images, but the contours again indicate SNRs above the threshold. This, again, can serve as an example of how easily a false detection can be made at such low SNR thresholds. The same is generally the case for HDFC0260, where the SNRs have been restructured and reshaped slightly. In the latter case, however, the peak SNR obtained through the new models is around 9% lower than that of the old models.

HDFC0262 is another bright source with the same general trend of the reorganisation of SNRs throughout the image. In this case, the SNR produced by the new

models was also higher than the old models by a few per cent, similar to HDFC0214. HDFC0277 echoes HDFC0260 with a lower SNR recorded by the new models than the old models. In both the fields where the old models seemingly outperformed the new models, the background regions in the images have higher emission levels. This may be due to MSSC not being performed or where these fields lie in the pointing FoVs.

6.2.5 How did the models perform?

There is still some ambiguity in the performance of the new models concerning intermediate SNR sources, such as HDFC0260, and further investigation is required to understand why the new models seem to have decreased SNRs for these sources. In extremely bright sources, such as HDFC0214 and HDFC0262, the new models have outperformed the old ones. This is a good indication, but the purpose of having accurate primary beam models is to expand the FoVs of pointings and thus increase the array's sensitivity in areas close to the HPBWs of the antennas. In these regions (see Figure 6.8), we could not obtain a strong conclusion that the new models outperformed the old models.

EG078B thus does not provide any comprehensive conclusion to the performance of the new versus the old models apart from bright sources obtaining higher SNRs. However, applying other advanced calibration techniques, such as MSSC, could change this. Additionally, the Lovell Telescope and Sheshan do not have new models, which restricts the expansion of the pointings offered by new models. It could still be the case that HDFA0013 and HDFA0017 lie outside of the HPBWs of the new models, especially since Effelsberg did not see a dramatic change from the old models to the new ones.

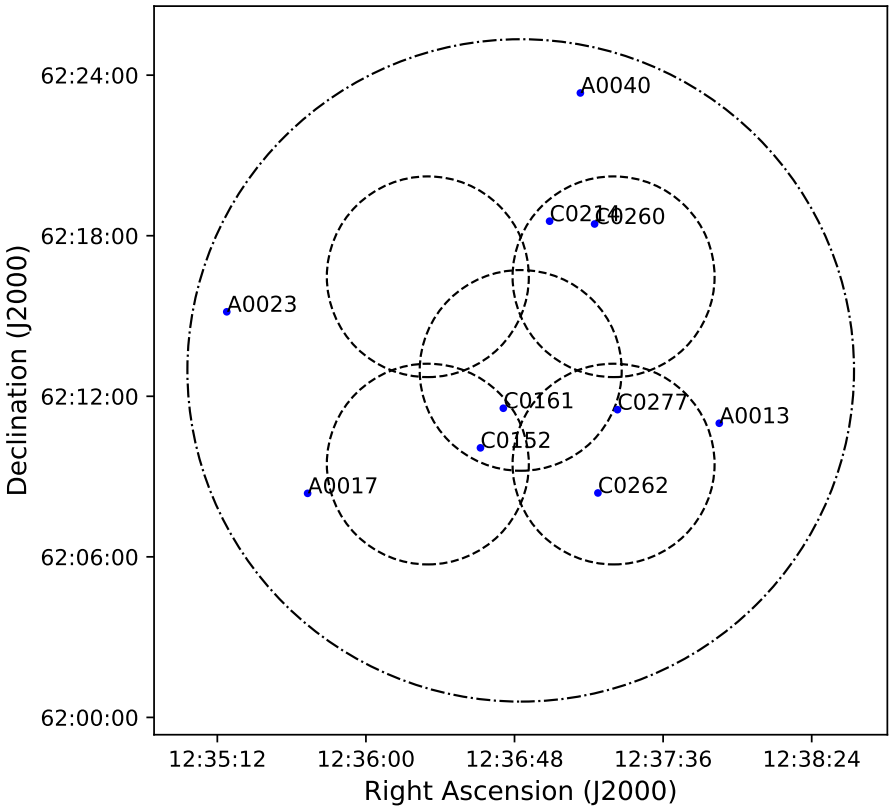

FIGURE 6.8: Pointings as shown in Figure 3.1 overlayed with the coordinates of the detections.

Chapter 7

Conclusion and Future Work

We have derived accurate primary beam models from ER052A for a large subset of the EVN and *e*-MERLIN arrays and supplemented them with models derived from N18L3. The antennas that use alt-azimuth mounts suffered from a parallactic angle dependence, but this did not cause substantial inaccuracies in most cases. However, it increased the spread in their required corrections generally, which potentially made their models slightly less accurate. Their relevant uncertainties are still relatively low, indicating that we can be confident in their accuracy. The models were applied to ER052A and essentially eliminated primary beam-induced attenuation within the HPBWs of the antennas, which again indicates high model accuracies.

Two antennas, Torun and Urumqi, experienced problems that made their models unviable. N18L3 was ideal to provide these antennas models and further expand the list of available models to be used on EG078B. The primary beam corrections derived for N18L3 had larger spreads generally than ER052A and larger uncertainties. Nonetheless, the models of the antennas missing from ER052A were deemed to have low enough statistical uncertainties and were accepted as somewhat accurate. The models of the larger antennas in this observation cannot be deemed accurate due to the low sampling density the large source position steps led to.

Auto-correlations can also be used to derive primary beam attenuation rates, but they were normalised during correlation in ER052A and were not included in N18L3. In the future, these should be used to derive alternative sets of models, as they are not dependent on baseline effects and constitute a direct measurement of the attenuation of the antenna primary beams. Additionally, emphasis should be placed on obtaining accurate models of the larger antennas in the network since they have the smallest FoVs and thus the most substantial limiting effects on observation FoVs.

An accurate model of Effelsberg is now available, but the rest of the large antennas still require their own. The ER052A-derived model of Tianma has roughly the same relationship between its real diameter and its effective diameter as Effelsberg, which is a good indication. This antenna was strongly affected by parallactic angle changes, which could be seen in the large spreads in its required corrections and the widespread in its corrections after applying the models to ER052A. Tianma was not included in EG078B and thus its model was not tested on data other than ER052A,

meaning its accuracy is still up for debate. The Lovell Telescope was included in both N18L3 and ER052A, but observational and suspected correlation problems caused its data to be flagged and thus not available for modelling. Sardinia was only included in N18L3 and had few attenuation measurements within its HPBW due to the low sampling density and thus cannot be used. Sheshan (65 m) was not included in ER052A nor N18L3, which means this station has no empirical model available. Without accurate models of the primary beams of these antennas, the EVN's FoV will always be restricted by them.

The newly derived models were compared to older and mainly non-empirical models by applying both generations to the EVN observation EG078B. The results were that the new models increased the SNRs of bright sources and decreased the SNRs slightly of the sources in the $\sim 7\sigma - 9\sigma$ range. The fields on the outskirts of the primary beams saw no substantial change, but their low brightnesses reduced the differences between the model generations, making detailed analysis difficult. MSSC was not applied during the calibration of the data of this observation, which may have led to lower SNRs in the data and thus far fewer detections being made here than by Radcliffe et al. (2018). This observation also has a complex pointing setup, increasing the difficulty of applying the models and performing subsequent analysis. Further tests of the models should be conducted in the future using wide-field observations with simpler observation schemes and, thus, potentially clearer differences between the models. We suggest that more models are derived before further detailed testing since the large antennas mostly do not have empirical models. For instance, the Lovell and Sheshan (65 m) telescopes are also included in EG078B and did not have new models.

The impact of these new models will only really be able to be gauged once they start to be used by astronomers on wide-field observations and in collaborations between the forthcoming Square Kilometer Array (SKA) and the SKA-VLBI observations (see Paragi et al., 2015). The SKA is the next generation of ultrasensitive radio telescope interferometer and should provide SNRs during SKA-VLBI observations that are high enough so that the new models will lead to improved source models and images. The data output rate of this array is also slated to be incredibly high and it presently is inclear which method of applying the primary beam models would be the best.

Bibliography

Artz, T, A Springer, and A Nothnagel (Dec. 2014). "A complete VLBI delay model for deforming radio telescopes: the Effelsberg case". In: *Journal of Geodesy* 88.12, pp. 1145–1161.

Barger, A. J. et al. (Aug. 2003). "Optical and Infrared Properties of the 2 Ms Chandra Deep Field North X-Ray Sources". In: *AJ* 126.2, pp. 632–665. DOI: 10.1086/376843. arXiv: astro-ph/0306212 [astro-ph].

Bhatnagar, S., U. Rau, and K. Golap (June 2013). "Wide-field wide-band Interferometric Imaging: The WB A-Projection and Hybrid Algorithms". In: *ApJ* 770.2, 91, p. 91. DOI: 10.1088/0004-637X/770/2/91. arXiv: 1304.4987 [astro-ph.IM].

Bhatnagar, S. et al. (2008). "Correcting direction-dependent gains in the deconvolution of radio interferometric images". In: *A&A* 487.1, pp. 419–429. DOI: 10.1051/0004-6361:20079284. URL: https://doi.org/10.1051/0004-6361:20079284.

Bianchi, Stefano, Roberto Maiolino, and Guido Risaliti (2012). "AGN Obscuration and the Unified Model". In: *Advances in Astronomy* 2012, p. 782030. ISSN: 1687-7969. DOI: 10.1155/2012/782030. URL: https://doi.org/10.1155/2012/782030.

Capak, P. et al. (Jan. 2004). "A Deep Wide-Field, Optical, and Near-Infrared Catalog of a Large Area around the Hubble Deep Field North". In: *AJ* 127.1, pp. 180–198. DOI: 10.1086/380611. arXiv: astro-ph/0312635 [astro-ph].

CASA Team (2022). "CASA, the Common Astronomy Software Applications for Radio Astronomy". In: *Publications of the Astronomical Society of the Pacific* 134.1041, p. 114501. DOI: 10.1088/1538-3873/ac9642. URL: https://dx.doi.org/10.1088/1538-3873/ac9642.

Casse, J. L. and C. A. Muller (Mar. 1974). "The Synthesis Radio Telescope at Westerbork. The 21 CM Continuum Receiver System". In: *A&A* 31, p. 333.

Chi, S., P. D. Barthel, and M. A. Garrett (2013). "Deep, wide-field, global VLBI observations of the Hubble deep field north (HDF-N) and flanking fields (HFF)". In: *A&A* 550, A68. DOI: 10.1051/0004-6361/201220783. URL: https://doi.org/10.1051/0004-6361/201220783.

Condon, J. J. and Scott M. Ransom (2016). *Essential radio astronomy*. eng. Princeton series in modern observational astronomy. Princeton: Princeton University Press Princeton. ISBN: 9780691137797; 069113779X.

Cornwell, T. J., K. Golap, and S. Bhatnagar (Dec. 2005). "W Projection: A New Algorithm for Wide Field Imaging with Radio Synthesis Arrays". In: *Astronomical*

Data Analysis Software and Systems XIV. Ed. by P. Shopbell, M. Britton, and R. Ebert. Vol. 347. Astronomical Society of the Pacific Conference Series, p. 86.

Deller, A. T. and E. Middelberg (Jan. 2014). "mJIVE-20: A Survey for Compact mJy Radio Objects with the Very Long Baseline Array". In: *AJ* 147.1, 14, p. 14. DOI: 10.1088/0004-6256/147/1/14. arXiv: 1310.8191 [astro-ph.CO].

Deller, A. T. et al. (Mar. 2007). "DiFX: A Software Correlator for Very Long Baseline Interferometry Using Multiprocessor Computing Environments". In: *PASP* 119.853, pp. 318–336. DOI: 10.1086/513572. arXiv: astro-ph/0702141 [astro-ph].

Deller, A. T. et al. (Mar. 2011). "DiFX-2: A More Flexible, Efficient, Robust, and Powerful Software Correlator". In: *PASP* 123.901, p. 275. DOI: 10.1086/658907. arXiv: 1101.0885 [astro-ph.IM].

Einstein, Albert (Jan. 1915). "Die Feldgleichungen der Gravitation". In: *Sitzungsberichte der Königlich Preussischen Akademie der Wissenschaften*, pp. 844–847.

Event Horizon Telescope Collaboration et al. (Apr. 2019). "First M87 Event Horizon Telescope Results. I. The Shadow of the Supermassive Black Hole". In: *ApJ* 875.1, L1, p. L1. DOI: 10.3847/2041-8213/ab0ec7. arXiv: 1906.11238 [astro-ph.GA].

Event Horizon Telescope Collaboration et al. (May 2022). "First Sagittarius A* Event Horizon Telescope Results. I. The Shadow of the Supermassive Black Hole in the Center of the Milky Way". In: *ApJ* 930.2, L12, p. L12. DOI: 10.3847/2041-8213/ac6674.

Garrett, M. A., J. M. Wrobel, and R. Morganti (2005). "Deep VLBI Imaging of Faint Radio Sources in the NOAO Bootes Field". In: *The Astrophysical Journal* 619.1, p. 105. DOI: 10.1086/426424. URL: https://dx.doi.org/10.1086/426424.

Garrett, M. A. et al. (Nov. 1999). "Wide-field VLBI imaging". In: *New Astron. Rev.* 43.8-10, pp. 519–522. DOI: 10.1016/S1387-6473(99)00045-7. arXiv: astro-ph/9906108 [astro-ph].

Garrett, M. A. et al. (2001). "AGN and starbursts at high redshift: High resolution EVN radio observations of the Hubble Deep Field". In: *A&A* 366.2, pp. L5–L8. DOI: 10.1051/0004-6361:20000537. URL: https://doi.org/10.1051/0004-6361:20000537.

Greisen, E. W. (Mar. 2003). "AIPS, the VLA, and the VLBA". In: *Information Handling in Astronomy - Historical Vistas*. Ed. by A. Heck. Vol. 285. Astrophysics and Space Science Library, p. 109. DOI: 10.1007/0-306-48080-8_7.

Hamaker, J. P. (2000). "Understanding radio polarimetry - IV. The full-coherency analogue of scalar self-calibration: Self-alignment, dynamic range and polarimetric fidelity". In: *Astron. Astrophys. Suppl. Ser.* 143.3, pp. 515–534. DOI: 10.1051/aas:2000337. URL: https://doi.org/10.1051/aas:2000337.

Hamaker, J. P., J. D. Bregman, and R. J. Sault (May 1996). "Understanding radio polarimetry. I. Mathematical foundations." In: *A&AS* 117, pp. 137–147.

Hardcastle, M. J. et al. (Oct. 2023). "The LOFAR Two-Metre Sky Survey. VI. Optical identifications for the second data release". In: *A&A* 678, A151, A151. DOI: 10.1051/0004-6361/202347333. arXiv: 2309.00102 [astro-ph.GA].

Heckman, Timothy M. and Philip N. Best (Aug. 2014). "The Coevolution of Galaxies and Supermassive Black Holes: Insights from Surveys of the Contemporary Universe". In: *ARA&A* 52, pp. 589–660. DOI: 10.1146/annurev-astro-081913-035722. arXiv: 1403.4620 [astro-ph.GA].

Herrera Ruiz, N. et al. (Sept. 2018). "VLBA+GBT observations of the COSMOS field and radio source counts at 1.4 GHz". In: *A&A* 616, A128, A128. DOI: 10.1051/0004-6361/201832969. arXiv: 1804.10464 [astro-ph.GA].

Högbom, J. A. (June 1974). "Aperture Synthesis with a Non-Regular Distribution of Interferometer Baselines". In: *A&AS* 15, p. 417.

Hogbom, J. A. and W. N. Brouw (July 1974). "The Synthesis Radio Telescope at Westerbork. Principles of Operation, Performance and Data Reduction". In: *A&A* 33, p. 289.

Holdaway, M. A. and Tamara T. Helfer (Jan. 1999). "Interferometric Array Design". In: *Synthesis Imaging in Radio Astronomy II*. Ed. by G. B. Taylor, C. L. Carilli, and R. A. Perley. Vol. 180. Astronomical Society of the Pacific Conference Series, p. 537.

Hsu, Li-Ting et al. (Feb. 2019). "Near-infrared Survey and Photometric Redshifts in the Extended GOODS-North Field". In: *ApJ* 871.2, 233, p. 233. DOI: 10.3847/1538-4357/aaf9a7. arXiv: 1901.00013 [astro-ph.GA].

Iheanetu, K. et al. (May 2019). "Primary beam effects of radio astronomy antennas - I. Modelling the Karl G. Jansky Very Large Array (VLA) L-band beam using holography". In: *MNRAS* 485.3, pp. 4107–4121. DOI: 10.1093/mnras/stz702. arXiv: 1903.02486 [astro-ph.IM].

Jagannathan, P. et al. (2017). "Direction-dependent Corrections in Polarimetric Radio Imaging. II. A-solver Methodology: A Low-order Solver for the A-term of the A-projection Algorithm". In: *The Astronomical Journal* 155.1, p. 3. DOI: 10.3847/1538-3881/aa989f. URL: https://dx.doi.org/10.3847/1538-3881/aa989f.

Kirsten, F. et al. (2022). "A repeating fast radio burst source in a globular cluster". In: *Nature* 602.7898, pp. 585–589. ISSN: 1476-4687. DOI: 10.1038/s41586-021-04354-w. URL: https://doi.org/10.1038/s41586-021-04354-w.

Leung, Calvin et al. (Mar. 2024). "A VLBI Software Correlator for Fast Radio Transients". In: *arXiv e-prints*, arXiv:2403.05631, arXiv:2403.05631. DOI: 10.48550/arXiv.2403.05631. arXiv: 2403.05631 [astro-ph.IM].

Marcote, B. et al. (2017). "The Repeating Fast Radio Burst FRB 121102 as Seen on Milliarcsecond Angular Scales". In: *The Astrophysical Journal Letters* 834.2, p. L8. DOI: 10.3847/2041-8213/834/2/L8. URL: https://dx.doi.org/10.3847/2041-8213/834/2/L8.

Marcote, B. et al. (2020). "A repeating fast radio burst source localized to a nearby spiral galaxy". In: *Nature* 577.7789, pp. 190–194. ISSN: 1476-4687. DOI: 10.1038/s41586-019-1866-z. URL: https://doi.org/10.1038/s41586-019-1866-z.

Marton, G. et al. (Aug. 2024). "The new Herschel/PACS Point Source Catalogue". In: *A&A* 688, A203, A203. DOI: 10.1051/0004-6361/202450032. arXiv: 2406.03116 [astro-ph.IM].

Martí-Vidal, I. et al. (2016). "Calibration of mixed-polarization interferometric observations - Tools for the reduction of interferometric data from elements with linear and circular polarization receivers". In: *A&A* 587, A143. DOI: 10.1051/0004-6361/201526063. URL: https://doi.org/10.1051/0004-6361/201526063.

McMullin, J. P. et al. (Oct. 2007). "CASA Architecture and Applications". In: *Astronomical Data Analysis Software and Systems XVI*. Ed. by R. A. Shaw, F. Hill, and D. J. Bell. Vol. 376. Astronomical Society of the Pacific Conference Series, p. 127.

Mezcua, M., A. P. Lobanov, and I. Martí-Vidal (Dec. 2013). "The resolved structure of the extragalactic supernova remnant SNR 4449-1". In: *MNRAS* 436.3, pp. 2454–2460. DOI: 10.1093/mnras/stt1738. arXiv: 1309.4013 [astro-ph.HE].

Middelberg, E. et al. (Feb. 2011). "Wide-field VLBA observations of the Chandra deep field South". In: *A&A* 526, A74, A74. DOI: 10.1051/0004-6361/201015406. arXiv: 1011.2400 [astro-ph.CO].

Middelberg, E. et al. (2013). "Mosaiced wide-field VLBI observations of the Lockman Hole/XMM". In: *A&A* 551, A97. DOI: 10.1051/0004-6361/201220374. URL: https://doi.org/10.1051/0004-6361/201220374.

Middelberg, Enno and Uwe Bach (2008). "High resolution radio astronomy using very long baseline interferometry". In: *Reports on Progress in Physics* 71.6, p. 066901. DOI: 10.1088/0034-4885/71/6/066901. URL: https://doi.org/10.1088/0034-4885/71/6/066901.

Morgan, J. S. et al. (Feb. 2011). "VLBI imaging throughout the primary beam using accurate UV shifting". In: *A&A* 526, A140, A140. DOI: 10.1051/0004-6361/201015775. arXiv: 1302.6040 [astro-ph.IM].

Morgan, John S. et al. (2013). "WIDE-FIELD VLBI OBSERVATIONS OF M31: A UNIQUE PROBE OF THE IONIZED INTERSTELLAR MEDIUM OF A NEARBY GALAXY". In: *The Astrophysical Journal* 768.1, p. 12. DOI: 10.1088/0004-637X/768/1/12. URL: https://dx.doi.org/10.1088/0004-637X/768/1/12.

Napier, P. J. (Jan. 1999). "The Primary Antenna Elements". In: *Synthesis Imaging in Radio Astronomy II*. Ed. by G. B. Taylor, C. L. Carilli, and R. A. Perley. Vol. 180. Astronomical Society of the Pacific Conference Series, p. 37.

Natarajan, Iniyan et al. (Feb. 2017). "Resolving the blazar CGRaBS J0809+5341 in the presence of telescope systematics". In: *MNRAS* 464.4, pp. 4306–4317. DOI: 10.1093/mnras/stw2653. arXiv: 1610.03773 [astro-ph.IM].

Netzer, Hagai (2015). "Revisiting the Unified Model of Active Galactic Nuclei". In: *Annual Review of Astronomy and Astrophysics* 53.1, pp. 365–408. DOI: 10.1146/

annurev-astro-082214-122302. eprint: https://doi.org/10.1146/annurev-astro-082214-122302. URL: https://doi.org/10.1146/annurev-astro-082214-122302.

Nimmo, K. et al. (2022). "Milliarcsecond Localization of the Repeating FRB 20201124A". In: *The Astrophysical Journal Letters* 927.1, p. L3. DOI: 10.3847/2041-8213/ac540f. URL: https://dx.doi.org/10.3847/2041-8213/ac540f.

Njeri, Ann et al. (Dec. 2022). "SPARCS-North Wide-field VLBI Survey: exploring the resolved μJy extragalactic radio source population with EVN + e-MERLIN". In: *Monthly Notices of the Royal Astronomical Society* 519.2, pp. 1732–1744. ISSN: 0035-8711. DOI: 10.1093/mnras/stac3569. eprint: https://academic.oup.com/mnras/article-pdf/519/2/1732/48447448/stac3569.pdf. URL: https://doi.org/10.1093/mnras/stac3569.

Oliphant, Travis E. (2006). *Guide to NumPy*. 2nd. USA: Trelgol Publishing.

Oliver, S. J. et al. (Aug. 2012). "The Herschel Multi-tiered Extragalactic Survey: HerMES". In: *MNRAS* 424.3, pp. 1614–1635. DOI: 10.1111/j.1365-2966.2012.20912.x. arXiv: 1203.2562 [astro-ph.CO].

Padovani, P. et al. (Aug. 2017). "Active galactic nuclei: what's in a name?" In: *A&ARv* 25.1, 2, p. 2. DOI: 10.1007/s00159-017-0102-9. arXiv: 1707.07134 [astro-ph.GA].

Paragi, Z. et al. (Apr. 2015). "Very Long Baseline Interferometry with the SKA". In: *Advancing Astrophysics with the Square Kilometre Array (AASKA14)*, 143, p. 143. DOI: 10.22323/1.215.0143. arXiv: 1412.5971 [astro-ph.IM].

Perley, Richard A. (Jan. 1999). "Imaging with Non-Coplanar Arrays". In: *Synthesis Imaging in Radio Astronomy II*. Ed. by G. B. Taylor, C. L. Carilli, and R. A. Perley. Vol. 180. Astronomical Society of the Pacific Conference Series, p. 383.

Popping, A. and Braun, R. (2008). "The standing wave phenomenon in radio telescopes - Frequency modulation of the WSRT primary beam". In: *A&A* 479.3, pp. 903–913. DOI: 10.1051/0004-6361:20079122. URL: https://doi.org/10.1051/0004-6361:20079122.

Radcliffe, J. F. et al. (Mar. 2016). "Multi-source self-calibration: Unveiling the microJy population of compact radio sources". In: *A&A* 587, A85, A85. DOI: 10.1051/0004-6361/201527980. arXiv: 1601.04452 [astro-ph.IM].

Radcliffe, J. F. et al. (2018). "Nowhere to Hide: Radio-faint AGN in GOODS-N field - I. Initial catalogue and radio properties". In: *A&A* 619, A48. DOI: 10.1051/0004-6361/201833399. URL: https://doi.org/10.1051/0004-6361/201833399.

Radcliffe, J. F. et al. (2021). "Nowhere to hide: Radio-faint AGN in the GOODS-N field - II. Multi-wavelength AGN selection techniques and host galaxy properties". In: *A&A* 649, A27. DOI: 10.1051/0004-6361/202038591. URL: https://doi.org/10.1051/0004-6361/202038591.

Radcliffe, Jack (Nov. 2020). *jradcliffe5/VLBI_pipeline: v0.5*. Version v0.5. DOI: 10.5281/zenodo.4288761. URL: https://doi.org/10.5281/zenodo.4288761.

Sarti, Pierguido, C Abbondanza, and L Vittuari (Nov. 2009). "Gravity-dependent signal path variation in a large VLBI telescope modelled with a combination of surveying methods". In: *Journal of Geodesy* 83.11, pp. 1115–1126.

Sarti, Pierguido, Monia Negusini, and Abbondanza Claudio (Feb. 2011). "Improved geodetic European very-long-baseline interferometry solution using models of antenna gravitational deformation". In: *Annals of Geophysics* 53, pp. 13–23. DOI: 10.4401/ag-4739.

Shimwell, T. W. et al. (Mar. 2022). "The LOFAR Two-metre Sky Survey. V. Second data release". In: *A&A* 659, A1, A1. DOI: 10.1051/0004-6361/202142484. arXiv: 2202.11733 [astro-ph.GA].

Silk, J., A. Di Cintio, and I. Dvorkin (2014). "Galaxy formation". In: *Proceedings of the International School of Physics “Enrico Fermi”* 186.New Horizons for Observational Cosmology, 137–187. ISSN: 0074-784X. DOI: 10.3254/978-1-61499-476-3-137. URL: https://doi.org/10.3254/978-1-61499-476-3-137.

Smirnov, O. M. (2011a). "Revisiting the radio interferometer measurement equation - I. A full-sky Jones formalism". In: *A&A* 527, A106. DOI: 10.1051/0004-6361/201016082. URL: https://doi.org/10.1051/0004-6361/201016082.

— (2011b). "Revisiting the radio interferometer measurement equation - II. Calibration and direction-dependent effects". In: *A&A* 527, A107. DOI: 10.1051/0004-6361/201116434. URL: https://doi.org/10.1051/0004-6361/201116434.

Spingola, C. (Jan. 2022). "Using strong gravitational lensing to zoom in on high-redshift galaxies". In: *European VLBI Network Mini-Symposium and Users' Meeting 2021*. Vol. 2021, 22, p. 22. DOI: 10.22323/1.399.0022. arXiv: 2112.05164 [astro-ph.GA].

Spingola, C et al. (May 2018). "SHARP – V. Modelling gravitationally lensed radio arcs imaged with global VLBI observations". In: *Monthly Notices of the Royal Astronomical Society* 478.4, pp. 4816–4829. ISSN: 0035-8711. DOI: 10.1093/mnras/sty1326. eprint: https://academic.oup.com/mnras/article-pdf/478/4/4816/26534518/sty1326.pdf. URL: https://doi.org/10.1093/mnras/sty1326.

Spingola, C. et al. (Feb. 2019). "A novel search for gravitationally lensed radio sources in wide-field VLBI imaging from the mJIVE-20 survey". In: *MNRAS* 483.2, pp. 2125–2153. DOI: 10.1093/mnras/sty3189. arXiv: 1811.09152 [astro-ph.GA].

Strom, R. (Jan. 2004). "What is the primary beam response of an interferometer with unequal elements?" In: *European VLBI Network on New Developments in VLBI Science and Technology*, pp. 273–274. DOI: 10.48550/arXiv.astro-ph/0412687. arXiv: astro-ph/0412687 [astro-ph].

Tasse, C. et al. (2018). "Faceting for direction-dependent spectral deconvolution". In: *A&A* 611, A87. DOI: 10.1051/0004-6361/201731474. URL: https://doi.org/10.1051/0004-6361/201731474.

Thompson, A. Richard, James M. Moran, and Jr. Swenson George W. (2017). *Interferometry and Synthesis in Radio Astronomy, 3rd Edition*. DOI: 10.1007/978-3-319-44431-4.

Thyagarajan, Nithyanandan et al. (Jan. 2017). "A generic and efficient E-field Parallel Imaging Correlator for next-generation radio telescopes". In: *Monthly Notices of the Royal Astronomical Society* 467.1, pp. 715–730. ISSN: 0035-8711. DOI: 10.1093/mnras/stx113. eprint: https://academic.oup.com/mnras/article-pdf/467/1/715/10493696/stx113.pdf. URL: https://doi.org/10.1093/mnras/stx113.

Uson, Juan M. and Cotton, W. D. (2008). "Beam squint and Stokes V with off-axis feeds". In: *A&A* 486.2, pp. 647–654. DOI: 10.1051/0004-6361:200809509. URL: https://doi.org/10.1051/0004-6361:200809509.

van Cittert, P.H (1934). "Die Wahrscheinliche Schwingungsverteilung in Einer von Einer Lichtquelle Direkt Oder Mittels Einer Linse Beleuchteten Ebene". In: *Physica* 1.1, pp. 201–210. ISSN: 0031-8914. DOI: https://doi.org/10.1016/S0031-8914(34)90026-4. URL: https://www.sciencedirect.com/science/article/pii/S0031891434900264.

Van Der Walt, Stefan, S Chris Colbert, and Gael Varoquaux (2011). "The NumPy array: a structure for efficient numerical computation". In: *Computing in Science & Engineering* 13.2, p. 22.

Venturi, Tiziana et al. (July 2020). "VLBI20-30: a scientific roadmap for the next decade – The future of the European VLBI Network". In: *arXiv e-prints*, arXiv:2007.02347, arXiv:2007.02347. arXiv: 2007.02347 [astro-ph.IM].

Virtanen, Pauli et al. (2020). "SciPy 1.0: Fundamental Algorithms for Scientific Computing in Python". In: *Nature Methods* 17, pp. 261–272. DOI: https://doi.org/10.1038/s41592-019-0686-2.

von Hoerner, Sebastian (Feb. 1967). "Design of large steerable antennas". In: *AJ* 72, p. 35. DOI: 10.1086/110198.

Xue, Y. Q. et al. (June 2016). "The 2 Ms Chandra Deep Field-North Survey and the 250 ks Extended Chandra Deep Field-South Survey: Improved Point-source Catalogs". In: *ApJS* 224.2, 15, p. 15. DOI: 10.3847/0067-0049/224/2/15. arXiv: 1602.06299 [astro-ph.GA].

Yang, G. et al. (Dec. 2014). "Photometric Redshifts in the Hawaii-Hubble Deep Field-North (H-HDF-N)". In: *ApJS* 215.2, 27, p. 27. DOI: 10.1088/0067-0049/215/2/27. arXiv: 1410.6860 [astro-ph.GA].

Zernike, F. (1938). "The concept of degree of coherence and its application to optical problems". In: *Physica* 5.8, pp. 785–795. ISSN: 0031-8914. DOI: https://doi.org/10.1016/S0031-8914(38)80203-2. URL: https://www.sciencedirect.com/science/article/pii/S0031891438802032.

Zhou, Bei et al. (2014). "Fast radio bursts as a cosmic probe?" In: *Phys. Rev. D* 89 (10), p. 107303. DOI: 10.1103/PhysRevD.89.107303. URL: https://link.aps.org/doi/10.1103/PhysRevD.89.107303.